4-2010

The Elemental Composition and the Spatial Distributions of Elements in the Crab Nebula

Timothy J. Satterfield
Trinity University, tsatterf@trinity.edu

THE ELEMENTAL COMPOSITION AND THE SPATIAL DISTRIBUTIONS OF ELEMENTS IN THE CRAB NEBULA

TIMOTHY J. SATTERFIELD

A DEPARTMENT HONORS THESIS SUBMITTED TO THE
DEPARTMENT OF PHYSICS AT TRINITY UNIVERSITY
IN PARTIAL FULFILLMENT OF THE REQUIREMENTS FOR GRADUATION WITH DEPARTMENTAL HONORS

DATE _____

_____ THESIS ADVISOR

_____ DEPARTMENT CHAIR

_____
ASSOCIATE VICE PRESIDENT FOR ACADEMIC AFFAIRS,
CURRICULUM AND STUDENT ISSUES

ABSTRACT

We present new observations and photoionization calculations for investigating gaseous regions that represent expected nuclear processing in the Crab Nebula supernova remnant. High helium abundance is shown to cause a very efficient [N II] $\lambda\lambda$6548,6583 emitting zone which can account for some strong nitrogen emission. This high helium abundance causes strong emission of [C I] $\lambda\lambda$9823,9850. When emission line measurements are compared with model simulations, most of the nebular gas appears to have depleted or solar nitrogen and enhanced carbon. This argues for a precursor star that had a mass greater than $9.5M_{\odot}$. We also use images of selected emission lines along with photoionization calculations to investigate the overall spatial distribution of elements in the Crab Nebula. We introduce new methods of calibrating direct images, including using existing Fabry-Perot data to take into account the different line-of-sight velocities of each individual filament. After processing, we compare these flux distributions with a large number of numerical model simulations to produce abundance maps of helium, nitrogen, oxygen, and sulfur in the Crab Nebula. These maps show evidence of gas that has undergone Carbon-Nitrogen-Oxygen processing, helium-burning, and oxygen-burning. High sulfur abundances mixed with gas representative of CNO processing were most likely generated from an off-center oxygen flash and then repositioned north and southeast from the pulsar by a relativistic wind. Clear evidence of oxygen burning material in the remnant gives strong support for a precursor star mass near $10M_{\odot}$.

Contents

1. Introduction

The heavy elements that make up our planet, such as the oxygen that we breathe or the carbon in our bodies, are all made in stars and may be dispersed through the mechanism of a supernova explosion. The Crab Nebula (M1 = NGC 1952) is generally recognized as the remnant of the core-collapse supernova SN1054. Estimates of the precursor star mass have previously been in the range of 8-12 $M_\odot$ (Davidson & Fesen 1985). The visible remnant contains at least 1-2 solar masses of gas, while the neutron star, which is the core of the original precursor star, has a mass of about 1.4 $M_\odot$ (MacAlpine & Uomoto 1991). The remaining mass may have been blown off by either a pre-supernova wind or a shockwave (Davidson & Fesen 1985).

The Crab Nebula is an ideal candidate for a study of stellar elemental processing stages. It is uncontaminated by interstellar debris due to its location far from the Galactic plane, as well as its young age (about 1000 years old as observed). Also, measured temperatures in the Crab Nebula indicate that it is ionized by its own synchrotron radiation field, instead of shock heating (see Appendix A.2). Thus, the ionization and the thermal properties may be accurately analyzed by using numerical photoionization codes.

More knowledge of the elemental and spatial composition of the Crab Nebula is important for delimiting the mass of the precursor star and determining whether the star underwent an O-Mg-Ne core collapse or an Fe core collapse. In addition, more detailed information about the composition and distribution of the elements should allow us to refine our current models of stellar evolution, especially in roughly 10 $M_\odot$ stars, and to understand better the dynamical details of the explosive process.

Just prior to exploding, the Crab Nebula's precursor star had elements left from different stages of nuclear processing. The expected element mass fractions for the different stages are shown in Fig. 1 for the case of a 15 $M_\odot$ star as a function of cumulative mass

radially away from the center. The first stage of processing that occurs in 10 $M_\odot$ stars is the CNO cycle, where hydrogen fuses into helium. Nitrogen is also enhanced in this stage because it acts as a catalyst to the fusion process. Thus, filaments that have products of this processing stage should have enhanced helium and nitrogen abundances (see interior mass in the 3.5 to 4.5 $M_\odot$ range in Fig. 1). After a star has processed most of its hydrogen, the helium-burning process begins. Because nearly all hydrogen has fused together to form helium, helium is expected to be even more enhanced than in the CNO processing zone. Helium nuclei are processed into oxygen and carbon, which are expected to be enhanced. Nitrogen should be either solar or depleted, due to helium fusing with nitrogen to become neon (see interior mass in the 2.5 to 3.5 $M_\odot$ range in Fig. 1). After helium burning is completed, oxygen begins to fuse in the oxygen-burning process. Oxygen fuses together to form silicon, sulfur, and argon, which are enhanced in areas where fusion stopped in this stage (see interior mass in the 1.5 to 2.5 $M_\odot$ range in Fig. 1). Determining what kind of processing happened in the precursor star should help us understand its mass.

A distinguishing property between a remnant from a precursor star with greater than 9.5 $M_\odot$ or less than 9.5 $M_\odot$ is the abundance of nebular carbon. However, previous attempts to study carbon in the Crab Nebula have been inconclusive. Some studies (e.g. Henry 1986) found carbon to be at solar levels or below, but they encountered problems with determining the source of [C I] λ9850 emission[1]. Other studies of C IV λ1549 and C III] λ1909 did not rule out excess carbon in the filaments, but could not provide enough evidence to support it either (Blair et al. 1992).

To address these questions about nebular carbon, we analyzed previously measured

[1]A line designation surrounded by brackets indicates forbidden emission, a line with only one bracket indicates semi-forbidden emission, and a line with no brackets surrounding it indicates allowed emission. Line measurements have units of Å.

spectra from selected positions to investigate elemental abundances at particular positions in the Crab Nebula using numerical photoionization simulations. We found that high helium abundances in filaments have substantial effects on ionization structure, which lead to strong collisionally-excited [C I]λ9850 emission. We also concluded that strong [N II]λ6583 does not imply high nitrogen abundance, while high [C I]λ9850 does imply high carbon abundance. These properties of the Crab Nebula argue consistently for a precursor star that had a mass greater than 9.5 $M_{\odot}$. This work is discussed in Sec. 2.

After finding this new limit on the mass of the precursor star, we then investigated the details of the supernova explosion by examining the spatial abundance distributions of different elements. To do this, we obtained new direct emission-line images of the Crab Nebula for multiple elements. In Sec. 3 we discuss our new data reduction techniques. Sec. 4 deals with the way we combined our observations with numerical photoionization models to map out the spatial distribution of helium, nitrogen, oxygen and sulfur in the Crab Nebula. We found that there is more CNO processing than first indicated by our work in Sec. 2, significant amounts of oxygen are in the nebula, indicating advanced stages of helium burning, and there is a substantial amount of sulfur surrounding the pulsar from oxygen burning. The distribution of sulfur suggests that it may have been deposited in the filaments by a relativistic wind.

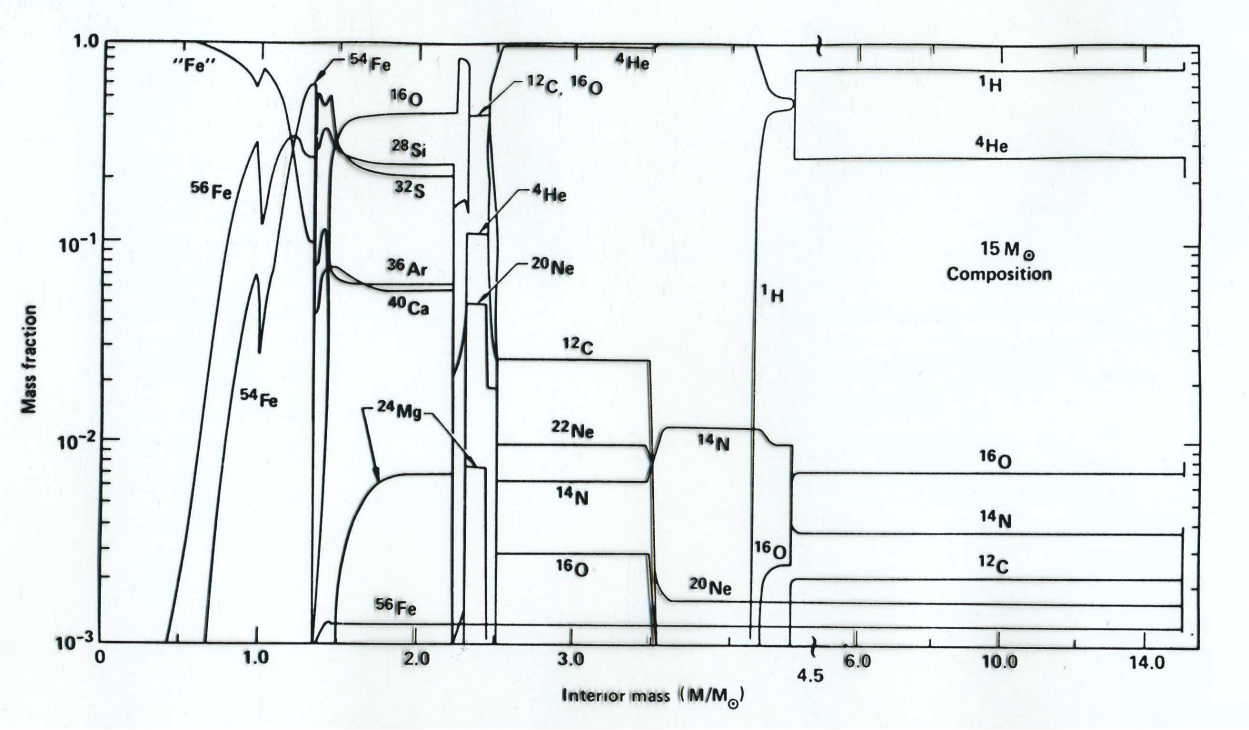

Fig. 1.— Theoretical elemental mass fractions for various nuclear processing stages in a 15 $M_\odot$ star (Woosley & Weaver 1995).

2. Matching Spectra to Photoionziation Models

Photoionization models were produced with the numerical code Cloudy, version 06.02c (Ferland et al. 1998). This photoionization code predicts physical conditions in various filaments in the Crab (including elemental ionization fractions, electron densities, and temperatures). Cloudy reads in three primary input parameters: the incident continuum illuminating the cloud, the chemical composition of the gas, and a stopping criterion. Using these inputs, Cloudy then simultaneously solves the equations of ionization and thermal equilibrium for the section of the cloud that is being hit by the incident radiation. After a consistent solution has been found, line emissivities and intensity ratios are calculated. The thermal, ionization and line-emission properties of the next zone (farther away from the source of incident radiation) are then determined in the same manner using the information from the previous zone, and the program continues to solve for zones deeper and deeper into the cloud until the stopping criterion is reached (in our case we used $T = 1000K$ as our stopping parameter).

Using the spectra observed by MacAlpine et al. (2007) and the correlations suggested in Figure 2 from MacAlpine et al. (2007), as well as stellar models of 15 $M_\odot$ stars shown in Figure 1 (from Woosley & Weaver 1995), three different domains of interest were identified (see MacAlpine & Satterfield 2008, hereafter Paper 1). The first domain showed high nitrogen emission, which would suggest processing that stopped with the CNO cycle. The second domain had lower nitrogen emission, along with elevated carbon emission, which suggests helium burning in the region. The third domain consisted of high sulfur and oxygen emission, along with low nitrogen emission. This was initially interpreted to be an oxygen burning region.

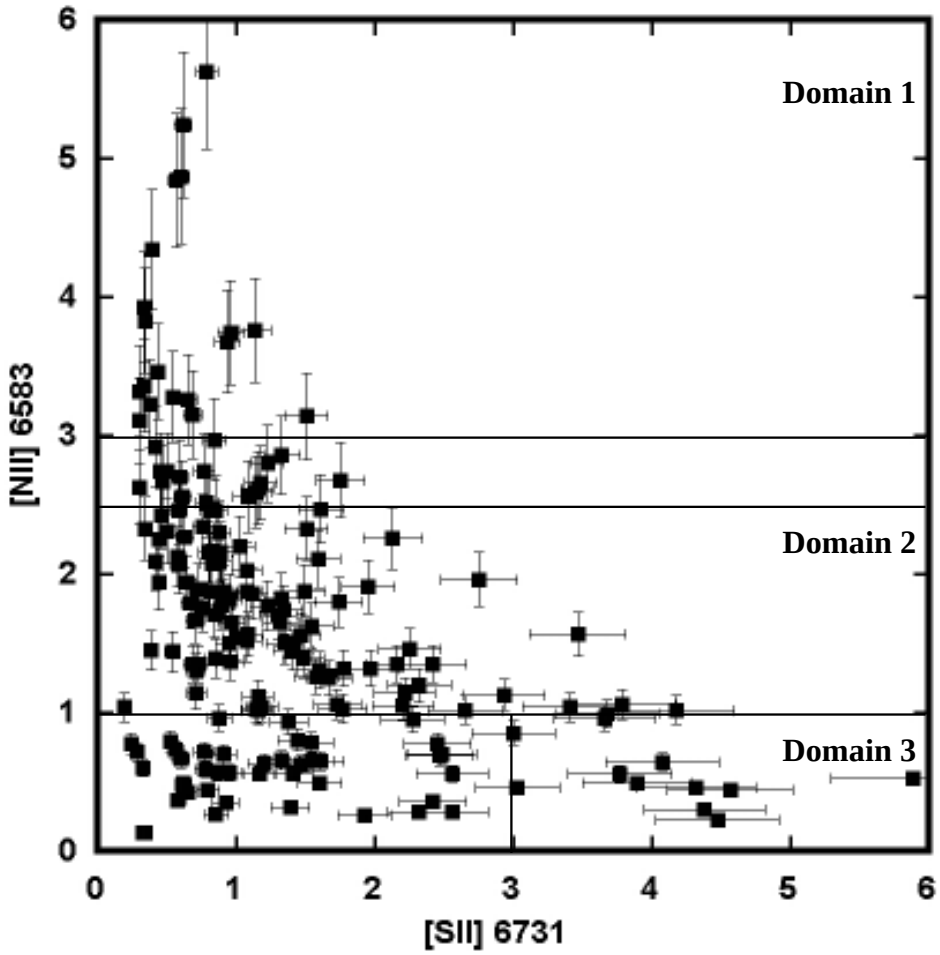

Fig. 2.— Correlation between Hα-normalized [N II]λ6583 and [S II]λ6731 measured line intensities from Figure 4 of MacAlpine et al. (2007). Investigated "gas domains" are indicated.

2.1. Experimentation with the Photoionization Code

Before attempts to match actual spectra to models using Cloudy, there was substantial experimentation with the different physical parameters to understand how they influenced the model output. Some of the most interesting physical parameters in the code include the hydrogen density, the ionization parameter, the ionizing spectrum, and the type of geometry of the filaments.

As the hydrogen density increases, the electron density rises because there are more easily ionizable atoms in the gas. Because the inferred mass is inversely proportional to the electron density, this is an important parameter for determining the total mass of the emitting filaments. Hydrogen densities also affect some emission lines, being directly correlated to the intensity ratio (relative to Hβ) of [O I],[C I], and [S II]. Thus, we determined that we needed to match observed electron densities (Fesen & Kirshner 1982) by manipulating the value of the hydrogen densities in the model.

The dimensionless ionization parameter is defined as U = Φ/cN, where Φ is the flux of photons more energetic than 13.6 eV striking the face of a cloud, c is the speed of light, and N is the number density of hydrogen. Raising the ionization parameter tended to raise the line intensity ratios relative to Hβ of doubly-ionized emission lines such as [O III] λ5007 and [S III] λ9069. On the other hand, the neutral emission lines such as [O I] λ6300 and [C I] λ9850 decreased in intensity as the ionization parameter rises. This is because, as more energy is incident on the cloud, it causes more atoms to become ionized and increases the number density of multiply ionized atoms, which generates stronger high ionization line emission. In addition, the electron densities and the temperatures of the filaments rose as we increased the ionization parameter. Although it affected so many different emission lines, it was found that the ionization parameter could be adjusted to obtain a consistent modeled emission-line spectrum that matches observations.

An ionizing spectrum that simulates the synchrotron emission in the Crab Nebula was also necessary in the simulation. While most of this spectrum is observed, there is an ultraviolet gap (see Figure 3, from Davidson & Fesen 1985). This gap allows for minor adjustments in the ionizing spectrum to help match certain lines. As the ionizing spectrum becomes more energetic, both the high and low ionization line ratios we investigated increased (high ionization lines saw a percentage change of about twice that of the lower ionization lines). Most importantly, the He II λ4686 line, which is not heavily affected by other parameters, increases as the ionization spectrum becomes more energetic. Thus, because it was the only parameter to affect He II emission, the values of the spectrum in the ultraviolet gap were selected mainly to match the output of the He II λ4686 line.

The geometry of the filaments was also considered. The three scenarios included a plane-parallel geometry where the radiation approaches the gas from one direction, cylindrical geometry where the ionizing synchrotron radiation approaches the filaments from all directions in one plane, and spherical geometry where the radiation approaches from all directions. Plane-parallel geometry tends to increase the intensities of the lines coming from neutral and singly ionized stages emitted deep inside the cloud. Cylindrical and spherical geometries enhance the high ionization lines that are produced near the edge of the cloud, where the radiation first hits. Going from plane-parallel to spherical geometry, the computed [S II] λ6731/Hα ratio could be reduced by as much as 30%, and [O I] λ6300/Hα ratio could be reduced by about 40%. Because the available Cloudy code only produces plane-parallel simulations, we altered it in order to investigate the other possible gas geometries.

After all of this experimentation, we adjusted the model input parameters and elemental abundances to obtain a satisfactory fit to observed median data. We decided to use a constant hydrogen density of 3000 cm^{-3} to match measured electron densities

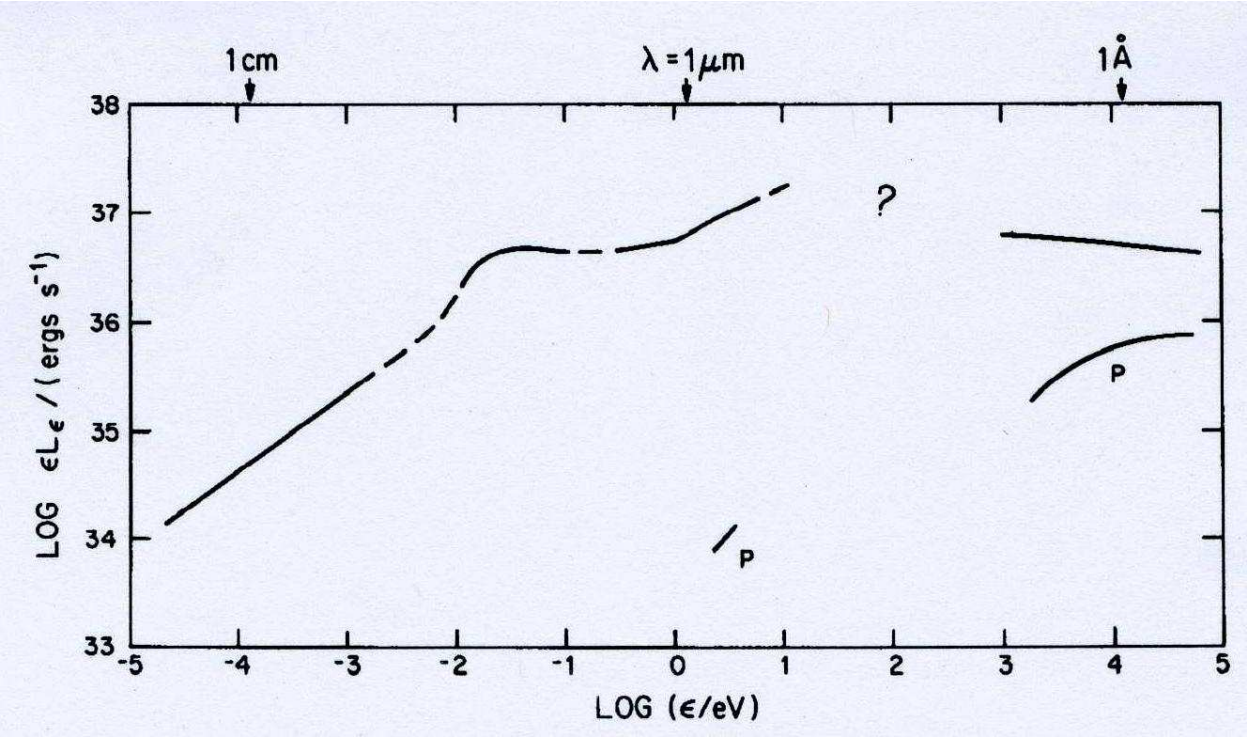

Fig. 3.— Ionizing emission spectrum of the Crab Nebula. Note the ultraviolet gap from 100 nm to 1 nm (Davidson & Fesen 1985).

(Fesen & Kirshner 1982), a log ionization parameter value of -3.2 to match the [S III] λ9069/[S II] λ6731 ratio, and an ionization spectrum provided by the Cloudy code, which was based on the observations of Davidson & Fesen (1985) with a linear integration over the unobserved portion, to match the He II λ4686/He I λ5876 ratio (MacAlpine et al. 1989). We then used these physical parameters to simulate the emission of filaments with different elemental abundances. We ran many different models that calculated the emission line ratios coming from each of these filaments. Our goal was to match the spectra that represented the three expected stellar elemental processing domains (an example spectrum is given in Figure 4). After examining the emission-line calculations coming from a model, we adjusted the parameters to come closer to exactly matching the spectrum. Once the model gave emission line ratios close enough to the observations (within 25% for every observed emission line), we were able to take the abundances from the model as representative of the overall elemental makeup of that region.

2.2. Domain 1: Strong Nitrogen Emission

For a representative "strong nitrogen emission" spectrum for comparison with model computations, we used spectra obtained by MacAlpine et al. (2007) to construct a median measured spectrum with Hα-normalized [N II] λ6583 values from 3.1 to 5.6. Due to the fact that we had no [C I] λ9850 measurements with [N II]/H$\alpha > 2.5$, we have no [C I] or [S III] measurements for this processing domain. Because of this, we *assumed* the carbon mass fraction to be 0.5 times solar, which is predicted by theory. The median measured spectrum and the modeled line intensities are shown in Table 1, and the calculated mass fractions of the elements of interest are shown in Table 2.

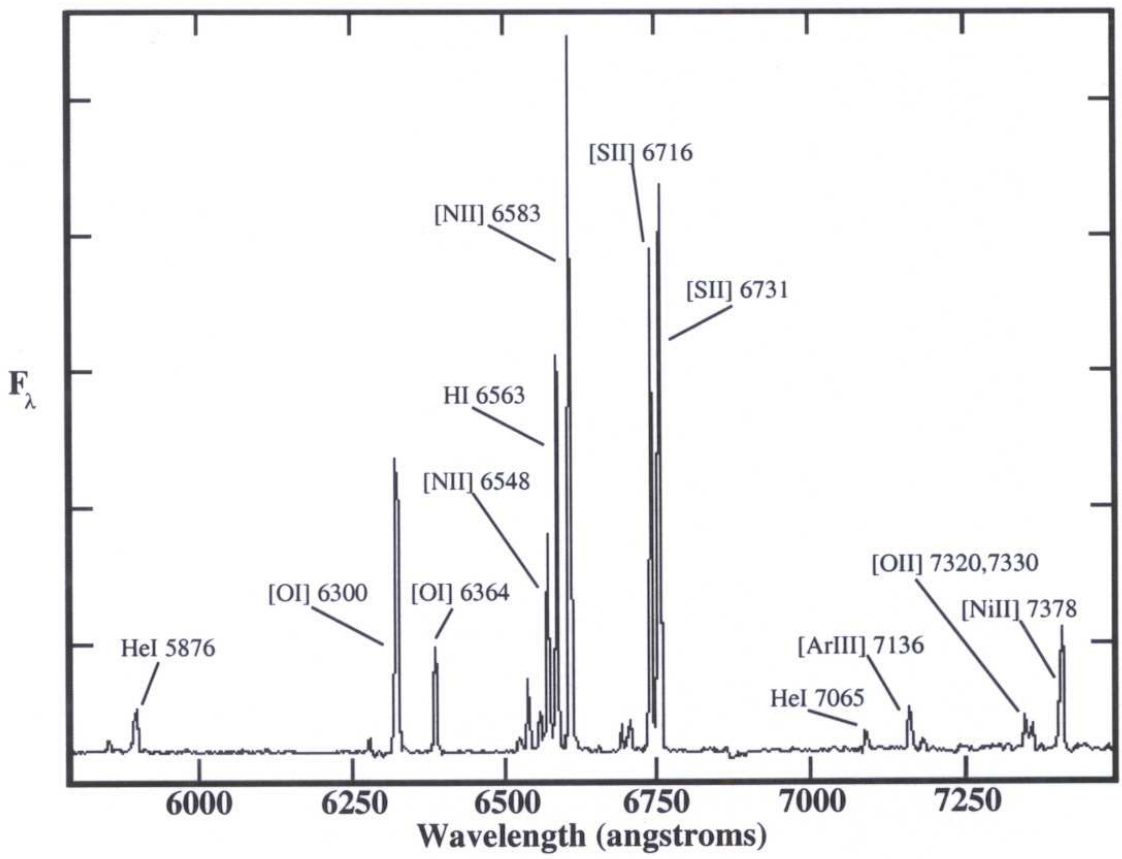

Fig. 4.— Sample optical spectrum with emission lines identified that were used for model comparisons. The vertical axis is relative flux density. From MacAlpine et al. (2007).

Table 1. Measured and Computed Line Intensity Ratios (From Paper 1)[a]

	Domain 1		Domain 2		Domain 3	
Line	Measured	Computed	Measured	Computed	Measured	Computed
He I λ5876	0.26	0.27	0.28	0.26	0.28	0.25
[O I] λ6300	0.40	0.41	0.32	0.34	0.58	0.44
[N II] λ6583	4.5	4.8	1.6	1.9	0.50	0.52
[S II] λ6731	0.64	0.66	0.85	0.82	4.0	3.6
[Ar III] λ7136	0.05	0.05	0.11	0.10	0.45	0.35
[S III] λ9069	—	0.22	0.26	0.27	0.83	0.90
[C I] λ9850	—	0.04	0.45	0.45	0.74	0.70

[a]Normalized to Hα.

Table 2. Deduced Element Mass Fractions (from Paper 1)

Element	Domain 1 Mass Fraction	Domain 2 Mass Fraction	Domain 3 Mass Fraction
Helium	89%	89%	89%
Nitrogen	solar	0.35 solar	0.28 solar
Carbon	0.50 solar	6 × solar	11 × solar
Oxygen	solar	solar	10 × solar
Sulfur	0.21 solar	0.28 solar	4 × solar
Argon	0.24 solar	0.55 solar	6 × solar

The helium mass fraction required to match the He I λ5876 emission is 89%, which is consistent for a region containing CNO processed materials. This large amount of helium in the filaments has significant effects on line emissions, particularly [N II] λ6583. Because of the high helium abundance, ionizing photons more energetic than 54.4 eV (the ionization potential of He^+) and 24.6 eV (the ionization potential of He^0) are absorbed by helium atoms before they can penetrate a substantial distance into the cloud. These zones are shown in Figure 5. Figures 5 & 6 show the modeled hydrogen, helium, carbon and nitrogen ionization for a region with 89% helium mass fraction. Because N^+ and N^0 ionization potentials are slightly above those of He^0 and H^0 respectively, high helium abundance causes a zone where N^+ can exist, along with neutral helium and ionized hydrogen. With the temperature and the electron density supporting collisional excitation, [N II] λ6583 is very efficiently produced. Thus, while previous studies (e.g. MacAlpine et al. 1996) proposed that strong [N II] indicates high nitrogen abundance and CNO processing, those investigations did not take into account the high helium abundance used here and its effects on nitrogen emission. Our numerical simulations show that the nitrogen mass fraction is only at its solar value. We also found that the oxygen was solar and sulfur was depleted. Assuming that carbon is also depleted, all of the elemental abundances match expectations for CNO processing gas except for nitrogen. Because of solar nitrogen, we suspect that there has been significant mixing of gases, or helium nuclei (α particles) were beginning to fuse with nitrogen, which depletes nitrogen and enhances neon.

2.3. Domain 2: Helium Burning

Our median observed spectrum representative of a helium-burning domain involved a subset of 19 spectra from MacAlpine et al. (2007) for which we had both optical and near-infrared measurements. For this, we used Hα-normalized [N II] λ6583 values from

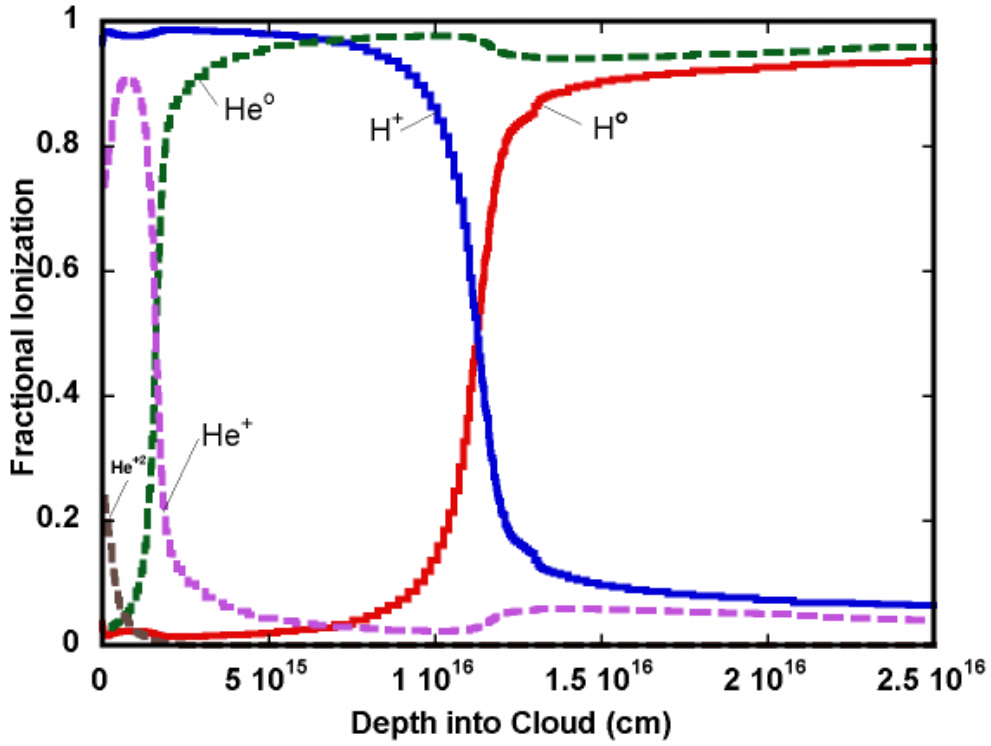

Fig. 5.— 89% He mass fraction hydrogen and helium ionization fractions as a function of distance into a cloud (from Paper 1).

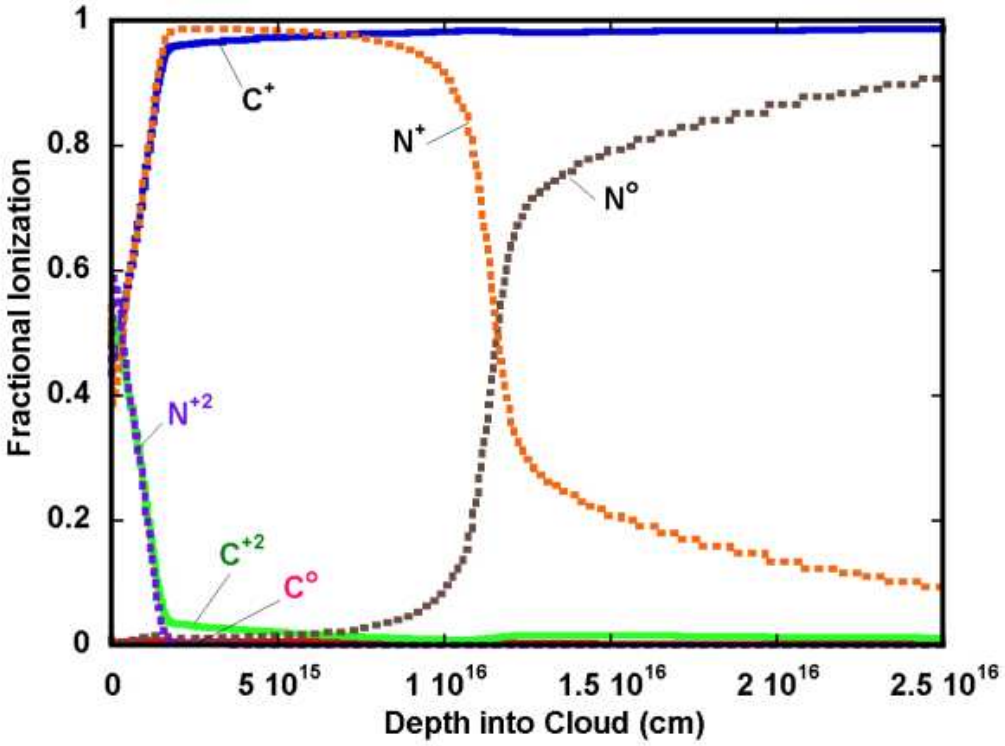

Fig. 6.— 89% He mass fraction modeled carbon and nitrogen ionization fractions as a function of distance into a cloud (from Paper 1).

1.0 to 2.5. These were chosen because, as helium burning occurs, nitrogen fuses with α particles to become neon, which weakens nitrogen emission.

As in Domain 1, the helium mass fraction was calculated to be 89% to match the observed He I λ5876 emission. Thus, the ionization structure of the cloud should be very similar to Domain 1. Domain 2 shows relatively high [C I] λ9850 emission. Because the C^+ ionization potential is comparable with that of He^0, and the ionization potential of C^0 is below that of H^0, the dominant ionization stage is C^+ from the He^+ zone to where the simulation stopped (see Figures 5 and 6, from Paper 1). Despite this, there is a small but significant peak of neutral carbon that exists where the electron density is high due to ionized helium (see Figure 7 and 8, from Paper 1). As the temperature decreases, there is a gradual increase of neutral carbon until we reach the hydrogen ionization edge, where there is virtually no neutral carbon because of the low electron density. The characteristics of the carbon are consistent with what would be expected from recombination of C^+ to C^0. [C I] λ9850 is then generated from electron collisional excitation of this neutral carbon.

Figure 9 shows selected line emissivities as a function of depth into a cloud. [N II] λ6583 emission is very high comparatively due to the electron collisional excitation in the [N II] emitting zone described in Section 2.2. H I λ6563 shows what we would expect from recombination, and [C I] λ9850 also shows a similar profile. Thus, we now understand that the [C I] λ9850 emission is coming from electron collisional excitation of C^0 generated by $C^+ \rightarrow C^0$ combination, and it is not due to high dielectronic recombination rates or collisional excitation by H^0 as previously postulated (Henry et al. 1984). We also note that [O I] λ6300 arises primarily from collisional excitation, and it is important in the neutral hydrogen region due to charge exchange processes between oxygen and hydrogen.

Table 2 lists the calculated mass fractions for this domain. We found that the nitrogen is about a third of its solar value, carbon is about six times solar, and oxygen is about solar.

This suggests that helium burning has taken place in this region, with little gas mixing having occurred.

2.4. Domain 3: Oxygen Burning

The selected spectra to make the representative spectrum for the strong sulfur emitting regions involved extreme cases with measured [S II] λ6731/Hα over the range 3-5.9 and with [N II] λ6583/Hα < 1. The measured median spectrum and computed line intensities for Domain 3 are also shown in Table 1. The best-fit photoionization model was similar to that described in section 2.1, except it was necessary in this case to lower the value of log ionization parameter to -3.5 to reproduce the measured [S III] λ9069/[S II] λ6731 ratio.

Like the other domains, the matched models indicate a helium mass fraction of about 89%, which would imply gas mixing for zones in which processing beyond helium burning had occurred. Nitrogen is depleted, and carbon and oxygen are enhanced (both by about ten times). As indicated by emissivity profiles shown in Figure 9, the observed correlation between [O I] λ6300 and [C I] λ9850 is an abundance effect, not an optical depth effect. The sulfur mass fraction is about four times solar, which confirms oxygen burning to have occurred in this region. This conclusion is also supported by the fact we see enhanced argon only in this domain, and not in Domains 1 and 2.

2.5. Summary

Previous studies (MacAlpine et al. 1996) have identified gas resulting from the CNO cycle and oxygen burning, with CNO cycle gas assumed to be the primary component, due to high nitrogen emission. However, our calculations have shown that strong [N II] λ6583 emission does not imply high nitrogen abundance. The result along with the fact that high

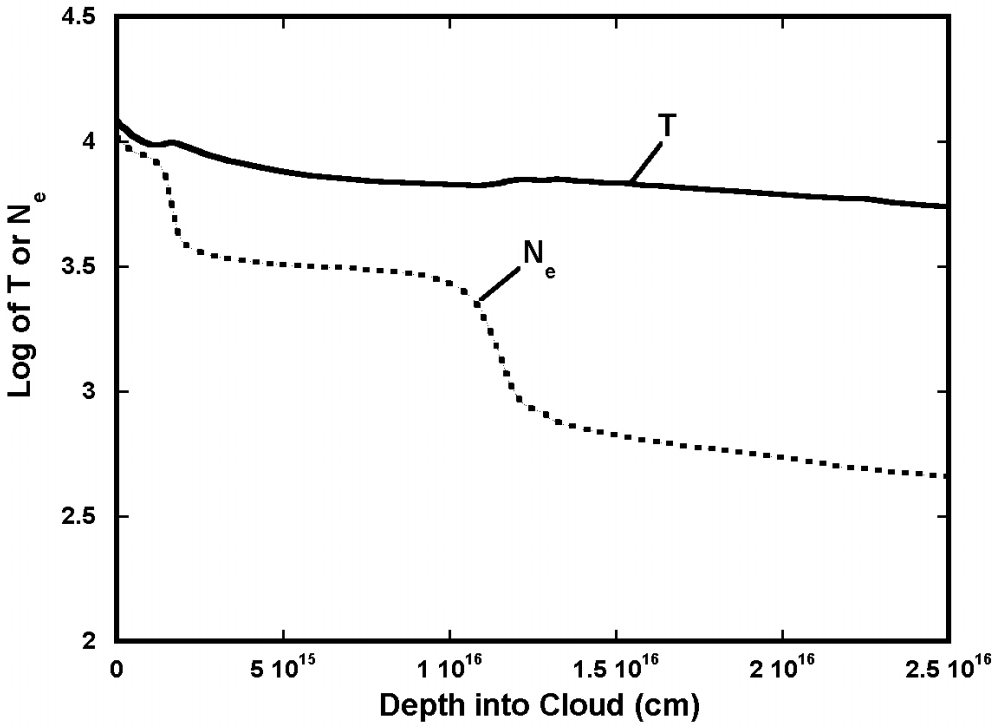

Fig. 7.— 89% He mass fraction modeled temperature (K) and electron density (cm^{-3}) as a function of distance into a cloud (from Paper 1).

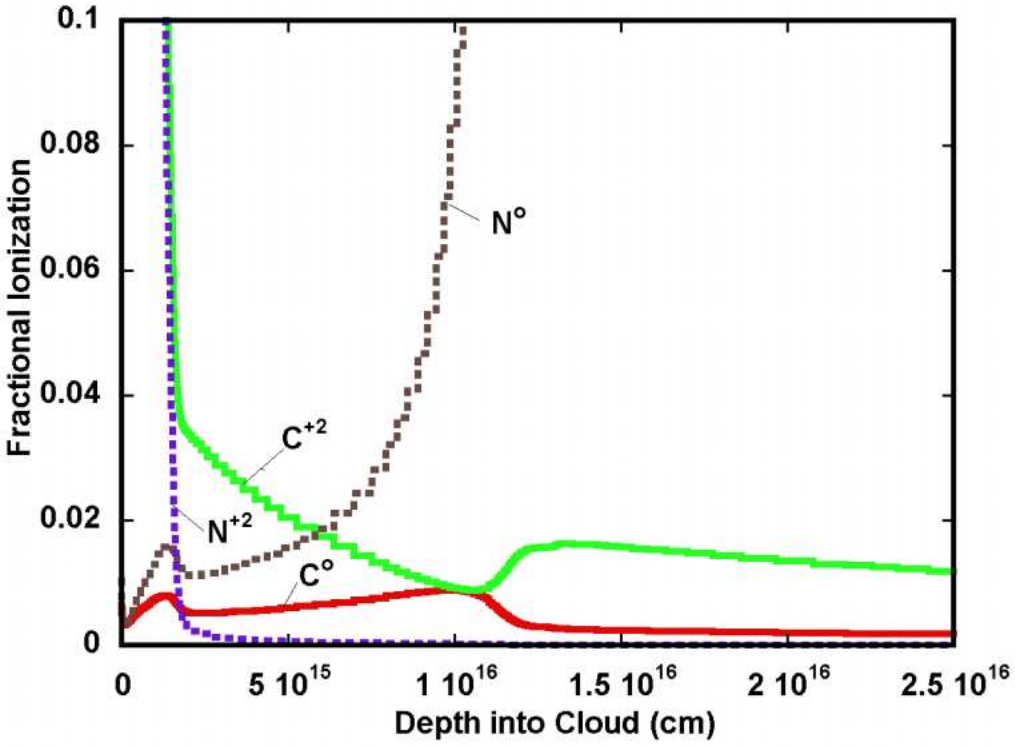

Fig. 8.— Expanded view of carbon and nitrogen ionization fractions below the value 0.1 on the vertical axis of Figure 7 (from Paper 1).

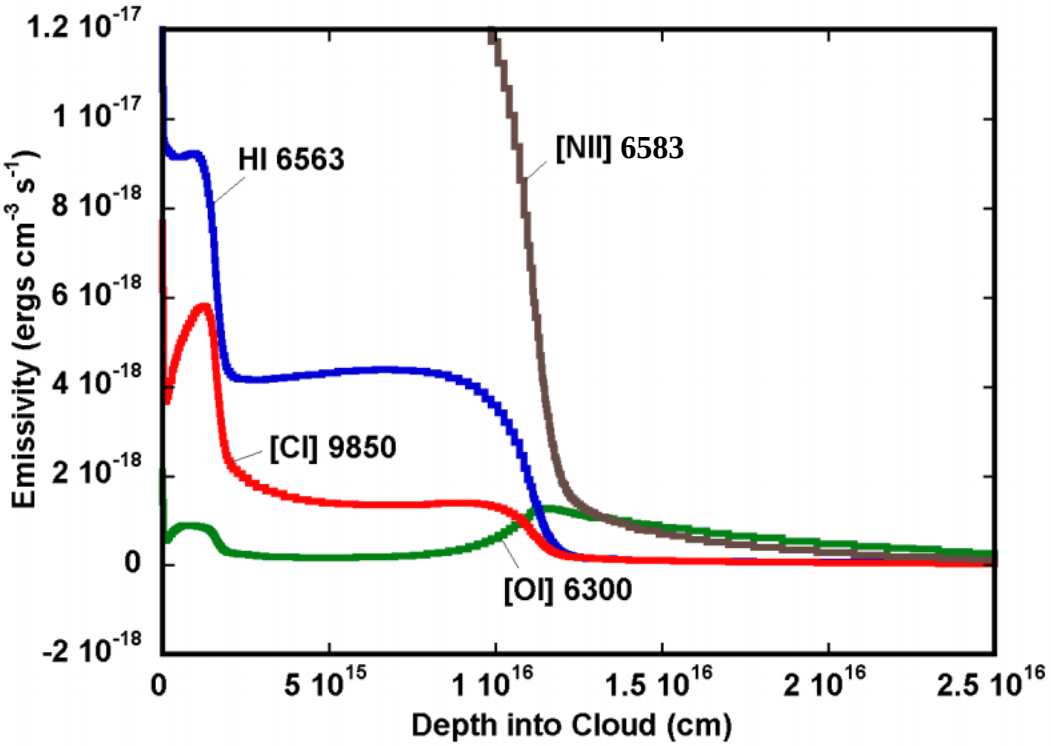

Fig. 9.— Selected Domain 2 line emissivities as a function of distance into a cloud (from Paper 1).

[C I] λ9850 emission implies high carbon abundance, suggests that most of the Crab Nebula is nitrogen depleted and carbon enhanced. This suggests that the precursor star had a mass > 9.5 $M_{\odot}$.

3. New Observations and Flux Calibration

To find out more about the spatial distribution of different elements and their geometry, we can combine abundance maps of the different elements with known nebular structure. To create these maps we needed direct images of the Crab Nebula in small wavelength bands corresponding to particular emission lines of certain elements. We obtained the imaging observations at MacDonald Observatory, on the 2.7m Harlan J. Smith telescope using the IGI imaging system and a 1024×1024 TK4 50-mm CCD camera. These observations were taken on the nights from December 1 2008 to December 4 2008. We observed the Crab Nebula through custom interference filters which took into account the rapid nebular expansion rate. These filters, provided by Omega Optical, isolated the lines of He II λ4686, Hβ, He I λ5876, [O I] $\lambda\lambda$6300,6364, [N II] $\lambda\lambda$6548,6583, [S II] $\lambda\lambda$6716,6731, and [Ni II] λ7378. We also observed the continuum emission from the Crab Nebula at the wavelengths of 5450 and 8050 angstroms and at least two calibrated standard stars for each filter. The transmission curves for these nine filters can be seen in Figure 10, 10b, and 10c. During our observations, we had relatively poor seeing, with a full width half maximum profile for stars of around 2.75 arcseconds for most of the night. After we took our data, we had images with the number of counts recorded by the CCD camera. However, before we could use the images for meaningful measurements, we had to put all the images through a data reduction process, which turned the counts into fluxes (ergs cm^{-2} sec^{-1}).

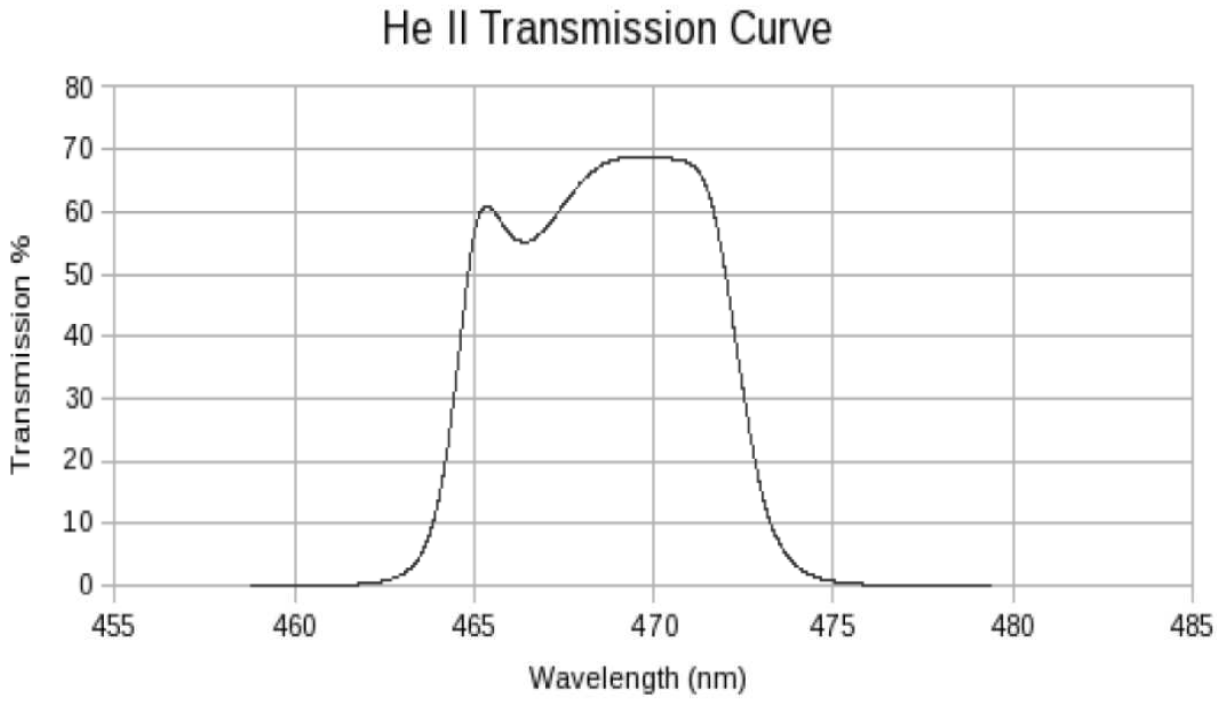

Fig. 10.— The transmission percentages of the filter isolating He II λ4686.

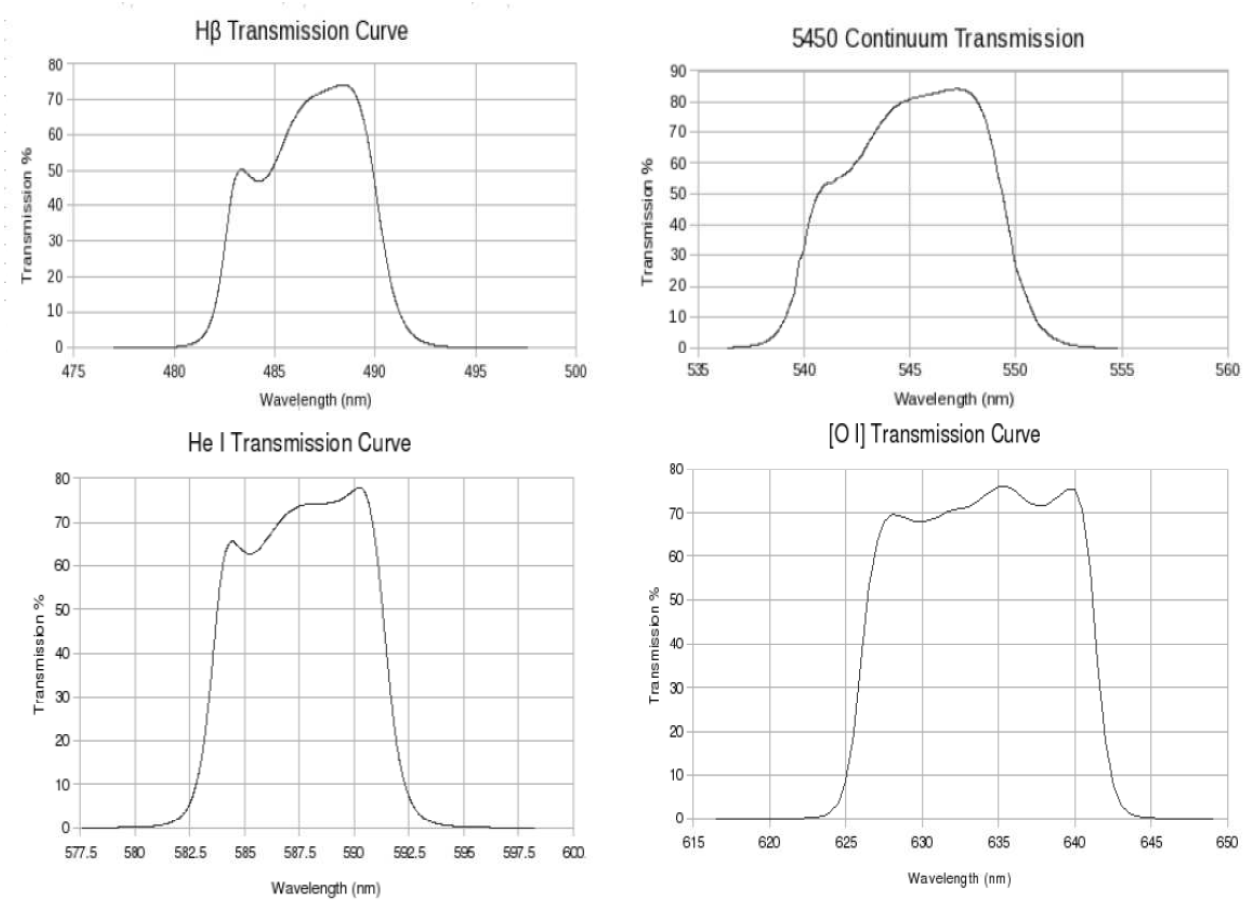

Fig. 10b.— The transmission percentages of four different filters isolating Hβ, 5450 Continuum, He I λ5876, and [O I] $\lambda\lambda$6300,6364.

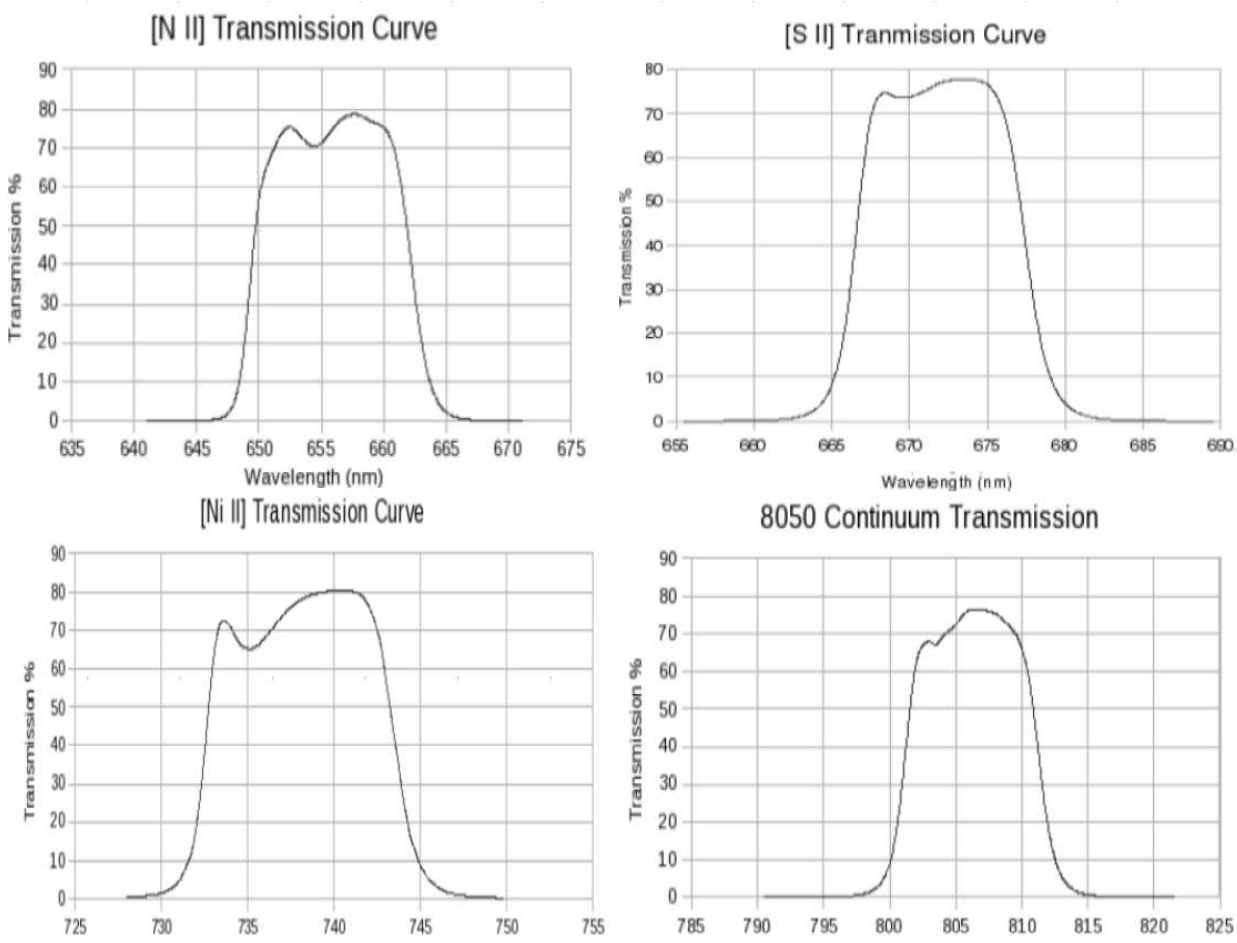

Fig. 10c.— The transmission percentages of four different filters isolating [N II] $\lambda\lambda$6548,6583, [S II] $\lambda\lambda$6716,6731, [Ni II] λ7378, and 8050 Continuum.

3.1. Removing Instrumental Signature and Registration

The first step in the data reduction process involved removing the instrumental signature from all the images. To eliminate the bias level structure (the inherent charge threshold on the CCD array) from the images, we took 21 zero second integration frames, averaged them together to reduce the detector noise, and then subtracted this averaged "zero frame" from each image. Individual bias levels were removed by subtracting the number of counts in the overscan region (pixels on the CCD that were not exposed to light during each individual observation) from each image. We also needed to remove the pixel-to-pixel variations on the CCD camera along with variations due to dust on the filters. We accomplished this by obtaining high signal-to-noise images of a uniformly lamp-illuminated dome flat through each filter, and then dividing these flat field images through all of the images corresponding to each filter. To remove all the cosmic ray hits from our images, we combined multiple exposures and median filtered them. Our integration times were short enough that dark current did not have a substantial impact on our observations. We performed all of these reductions using the *ccdproc* routines in the IRAF software (Tody 1986). Because we were working with relatively short wavelengths, "fringing corrections" were not necessary for our reduction procedure.

To deal with seeing effects, we placed a 3×3 pixel box around each pixel, and averaged all of those values together. This allows for meaningful comparison of pixel by pixel measurements in our images even though the seeing was variable.

We then moved on to registering the images (i.e. adjusting so the same pixel number in each image corresponds to the same astronomical coordinates). For reasons that will become apparent, we decided to register our observations with the images from the Fabry-Perot datacube found in Lawrence et al. (1995). First, we lined up the median filtered observations, using the IRAF routine *geomap*. Employing our 5450 continuum

image as our reference, we chose from 10 to 16 stars as reference points in each frame and used those coordinates to calculate the necessary shifts and rotations that needed to be applied. After the initial registrations, we ended up with a maximum residual of around 0.5 pixels (most values were within 0.1 pixels). After registering all of our images, we mapped out the 5450 continuum (and thus all the other observations) in right ascension and declination so we could calculate how our pixel positions corresponded to pixel coordinates in the Fabry-Perot images. We first visually identified four reference stars. Using the right ascension and declination coordinates from the United States Naval Observatory A star catalog, we were able to make a first approximation. We used the initial solution in conjunction withe the IRAF routine *ccfind* to locate 11 more additional reference stars, and using those we were able to create an improved solution. The RMS for the second solution was about 0.2 arcseconds, which is close to the lower RMS limit due to scatter in the USNOA catalog. Using this information, we converted the pixel values for both the observations and the Fabry-Perot images into right ascension and declination. We then used 12 pixels that had the same right ascension and declination in another run of *geomap*, and employed the output of that routine to register our images to the Fabry-Perot images for calibration.

3.2. Sensitivity Calculations

Since we observed standard stars with known flux distributions, we could derive the absolute sensitivity of our telescope and detector system. When we convolved the stellar fluxes with the transmission curve coefficients, we were able to relate count rates in our images to actual flux coming from the nebula. We used a method similar to the one described in Jacoby et al. (1987). We obtained transmission curves and traces from our filter manufacturers, Omega Optical. From published literature, we had known

monochromatic fluxes above the atmosphere for the standard stars, but not all of that flux could be measured by the system due to the presence of the atmosphere and absorption by the transmission filter. Neglecting atmospheric absorption, the total stellar flux (in ergs cm^{-2} sec^{-1}) incident on the detector can be described by the equation

$$F(i) = \int F_\lambda T_\lambda d\lambda, \tag{1}$$

where T_λ represents transmission as a function of wavelength for the ith filter, and F_λ is the flux directly above the atmosphere from the star, measured in ergs cm^{-2} s^{-1} $Å^{-1}$. The system sensitivity, which takes into account things like detector response and telescope optics, can be obtained by the equation

$$S(i) = \frac{F(i)}{C10^{0.4k(i)A}}, \tag{2}$$

where C is the count rate measured in the image, k(i) is the airmass extinction coefficient in magnitudes per airmass, and A is the airmass [measured by *sec(z)*, where z is the observing angle measured relative to the zenith]. Observing at the zenith (z=0°) would give an airmass of one. Assuming delta functions for the nebular emission lines from individual gas locations, and with multiple sensitivity values derived from several standard stars using equation 2, we can represent the flux coming from any region in the nebula by using the equation

$$F_N(i) = \frac{< S(i) > C_N 10^{0.4k(i)A}}{T_\lambda}. \tag{3}$$

After searching for software that would perform the calibration and calculate the desired sensitivity values, we found none and decided to write our own computer code. Our first step was to approximate the integral of total observable flux as a trapezoidal sum. To do this, we used the monochromatic fluxes for each of the standard stars in Oke (1990). The wavelength interval depended on the standard star, as the monochromatic flux intervals dλ provided by the literature were different. In some cases, we had to make an extra

assumption that the flux was constant over the wavelength interval (a maximum of 50 Å) so that we could take into account the shape of the transmission curve. For this assumption, the flux equation is

$$F(i) = F_\lambda \int T_\lambda d\lambda. \tag{4}$$

After using our code to determine the flux, we employed the IRAF package *digiphot* to obtain the count rates (the amount of counts registered by the CCD camera per second) in the standard stars. For seeing of about 2.5 arcseconds, we used a simulated aperture of 17.5 arcseconds, so that most of the standard star light is included in the measurement. We determined the sky value for each image by averaging four different regions in each image that were free of nebular emission. The airmass present at observing was recorded in the image header, and we approximated the airmass extinction coefficients by using the values from the Kitt Peak National Observatory (see Massey & Foltz 2000). Since the coefficients changed only slightly over most of our bandpasses, we took the average value on the interval to serve as the airmass extinction for equation 2. The calculated sensitivity values for each standard star are listed in Table 3. These sensitivity values agree to within 10% within each filter subgroup, and thus we determined that the sensitivities are valid.

3.3. Continuum Subtraction

After successfully registering the images and determining the system sensitivity, our next step was to use the images of the continuum at both 5450 and 8050 angstroms to subtract off the non-filament continuum flux contributions. Because this background is not a delta function like an emission line, calculating the flux from equation 3 was invalid. However, by making the assumption that continuum emission was constant in the small bandpass of each filter we were able to modify equation 3 to

$$F_C(i) = \frac{< S(i) > C_C 10^{0.4k(i)A}}{\int T_\lambda d\lambda}. \tag{5}$$

Table 3. Sensitivity Calculations

Filter	Standard Star	Sensitivity
He II λ4686	Hiltner 600	8.37×10^{-16}
He II λ4686	G191-B2B	8.27×10^{-16}
Hβ	Feige 110	7.39×10^{-16}
Hβ	G158-100	7.20×10^{-16}
5450	Feige 110	3.93×10^{-16}
5450	G158-100	3.71×10^{-16}
He I λ5876	Feige 110	6.07×10^{-16}
He I λ5876	G158-100	6.48×10^{-16}
[O I] $\lambda\lambda$6300,6364	Feige 34	5.20×10^{-16}
[O I] $\lambda\lambda$6300,6364	Hiltner 600	5.63×10^{-16}
[N II] $\lambda\lambda$6548,6583	G191-B2B	4.57×10^{-16}
[N II] $\lambda\lambda$6548,6583	G158-100	4.75×10^{-16}
[S II] $\lambda\lambda$6716,6731	G191-B2B	4.71×10^{-16}
[S II] $\lambda\lambda$6716,6731	G158-100	4.85×10^{-16}
[Ni II] λ7378	Feige 110	6.70×10^{-16}
[Ni II] λ7378	G158-100	6.50×10^{-16}
8050	Feige 34	8.32×10^{-16}
8050	Hiltner 600	8.85×10^{-16}

Note. — The standard stars observed through each interference filter, and their respective sensitivity values are in ergs cm^{-2} count^{-1}.

In this equation C_C is the counts contributed from the entire bandpass, and not solely the contribution from one emission line. This expression also takes into account values of the entire transmission curve rather than just a transmission value at a single wavelength, like in equation 3. We applied equation 5 to each observed continuum image to find the flux background contribution at the two observed wavelengths. The 5450 continuum and the 8050 flux were weighted to find the local background contributed at each observed wavelength. We determined the initial weights of each image using the equation

$$w_{5450}(\lambda) = \frac{8050\mathring{A} - \lambda}{2600\mathring{A}}, w_{8050}(\lambda) = \frac{\lambda - 5450\mathring{A}}{2600\mathring{A}}, \tag{6}$$

where λ is the wavelength of the emission line of interest, and 2600 Åis the total separation of the two continuum observations in wavelength space. Background subtractions were then made from each line-emission image. We applied an adjustment factor (not exceeding 10%) to account for slight overestimates or underestimates of background contributions. Visual inspection of the subtracted images showed that this process worked well, except for the cases of He II λ4686 and Hβ. For these lines, we changed the weights of the two continuum images until the background subtraction was satisfactory. Oddly enough, the best weighted continuum had no contributions from the 5450 image, which is much closer in wavelength space. The final weighting coefficients for all other emission lines were the values calculated in equation 5 multiplied by the weights determined by equation 6. These weights can be found in Table 4. After background subtraction was made from the emission line images, we recalibrated from counts to flux using the methods in Section 3.2.

3.4. Velocity Profiling

While we designed our filters to take into account the expansion rate of the Crab Nebula as a whole, the expansion velocities of different filaments vary with position across the nebula. In addition, in our line of sight, there could be multiple filaments moving at

Table 4. Continuum Scaling

Filter	5450 Coefficient	8050 Coefficient	Adjustment Factor
He II λ4686	0	0.777	1
Hβ	0	0.757	1
He I λ5876	0.541	0.197	1.05
[O I] $\lambda\lambda$6300,6364	0.708	0.640	1
[N II] $\lambda\lambda$6548,6583	0.499	0.704	1.1
[S II] $\lambda\lambda$6716,6731	0.254	0.460	1
[Ni II] λ7378	0.148	0.667	1.1

Note. — The amount of 5450 and the 8050 continuum subtracted from images in each filter, along with the adjustment ratios.

different velocities emitting radiation at any given pixel. Doppler shifting for differing line-of-sight velocities will cause radiation at each pixel to be distributed in a particular way across the non-uniform filter transmission curves. To take this into account, we used the 27 [O III] λ5007 Fabry-Perot images in Lawrence et al. (1995). We examined each pixel of these images and determined which velocities contained enough signal to be considered significant (we used a cutoff of 2*10^{-17} ergs cm^{-2} s^{-1}). After ignoring the pixels that do not have enough signal, we found the ratio of the signal in one image over the total signal in all 27 images for each pixel. Using these weights, we constructed a line-of-sight velocity (and wavelength) distribution for each pixel in our images. Assuming the velocity distribution of the [O III] λ5007 emission is identical to the distributions of our observed emission lines, we can use the equation

$$F_N(i) =< S(i) > C_N 10^{0.4k(i)A} \sum \frac{w_n}{T_{\lambda,n}} \tag{7}$$

to determine the flux of each singlet line, where $T_{\lambda,n}$ is the transmission coefficient for a redshifted or blueshifted emission line, and w_n is the ratio of flux in one frame to the entire summed flux in that pixel, determined from the Fabry-Perot images. For doublets with wavelengths λ and λ', the equation changes slightly to

$$F_N(i) =< S(i) > C_N 10^{0.4k(i)A} \sum x\frac{w_n}{T_{\lambda,n}} + (1-x)\frac{w_n}{T_{\lambda',n}} \tag{8}$$

where x is the ratio of emission that one line of the doublet contributes to total emission. We assumed that the emission ratios stay the same throughout the Crab Nebula. For the unique case of [N II] $\lambda\lambda$6548,6583, which is substantially contaminated by Hα, we first calculated the total Hβ flux, scaled the flux at each pixel by 2.71 to determine the flux from Hα, and transformed this flux into counts by using equation 6. We then subtracted these counts from the [N II] $\lambda\lambda$6548,6583 image and used that subtracted value for C_N in equation 7.

3.5. Conclusions and Final Images

After performing reddening corrections with a color excess $E_{(B-V)}$=0.47, and a magnitude of absorption in the visual band A_{ν}=1.457, we had fully completed our processing routines. Our total Hβ flux (the amount of total flux coming from the Crab Nebula observed above the Earth's atmosphere) was 1.61*10^{-11} ergs cm^{-2} sec^{-1}, and this agrees reasonably well with previous photometry by MacAlpine & Uomoto (1991), who measured 1.78*10^{-11} ergs cm^{-2} sec^{-1}. Thus, our processes appear to be valid, and our images are able to yield accurate spatial abundance maps when combined with grids of photoionization models. The final flux images are Figures 11-17. The bright and dark rings seen in the images are star subtractions. Bright streaks to the left of the Crab Nebula in some images are light leaks from the filter.

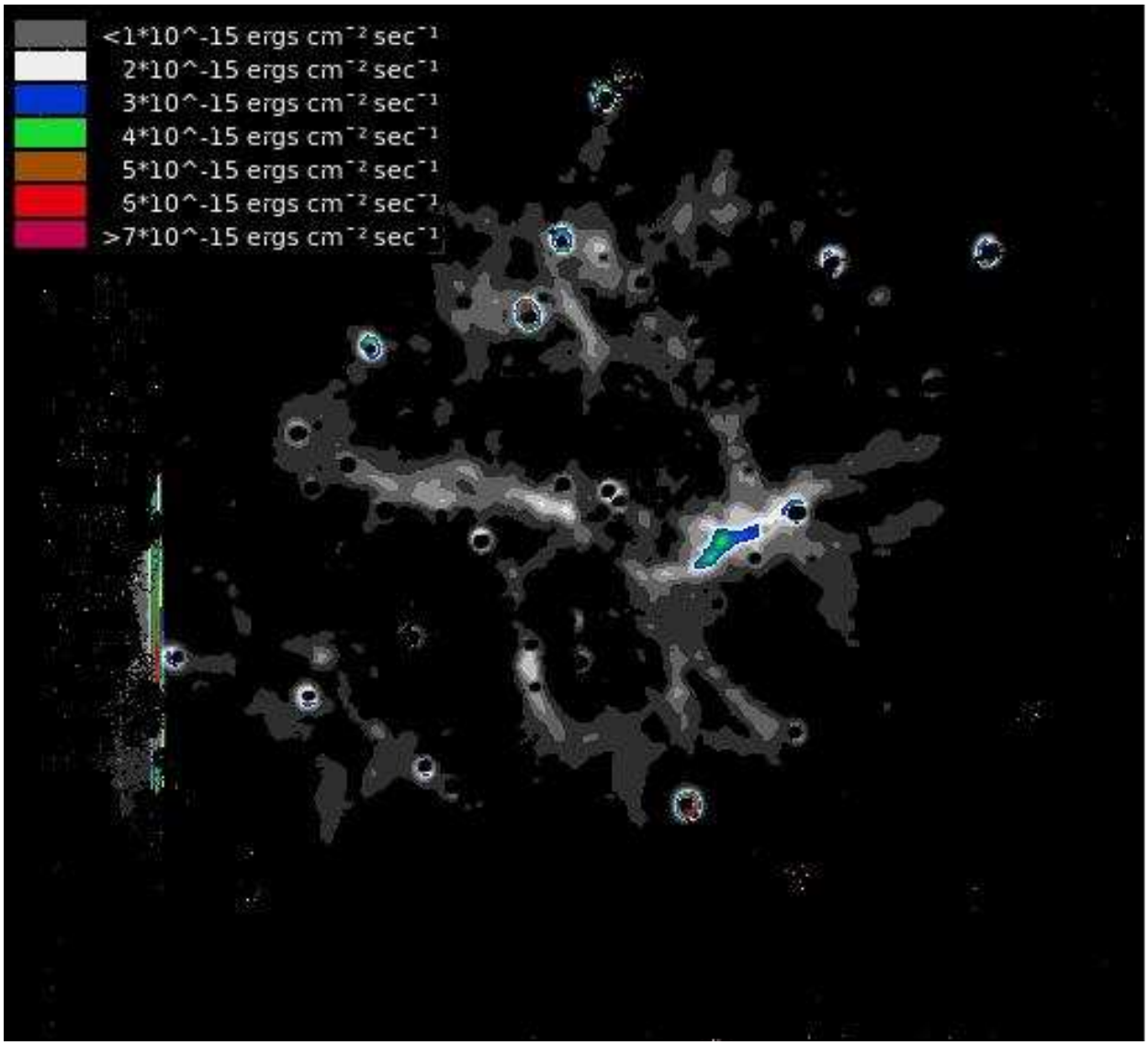

Fig. 11.— Flux Image of He II λ4686.

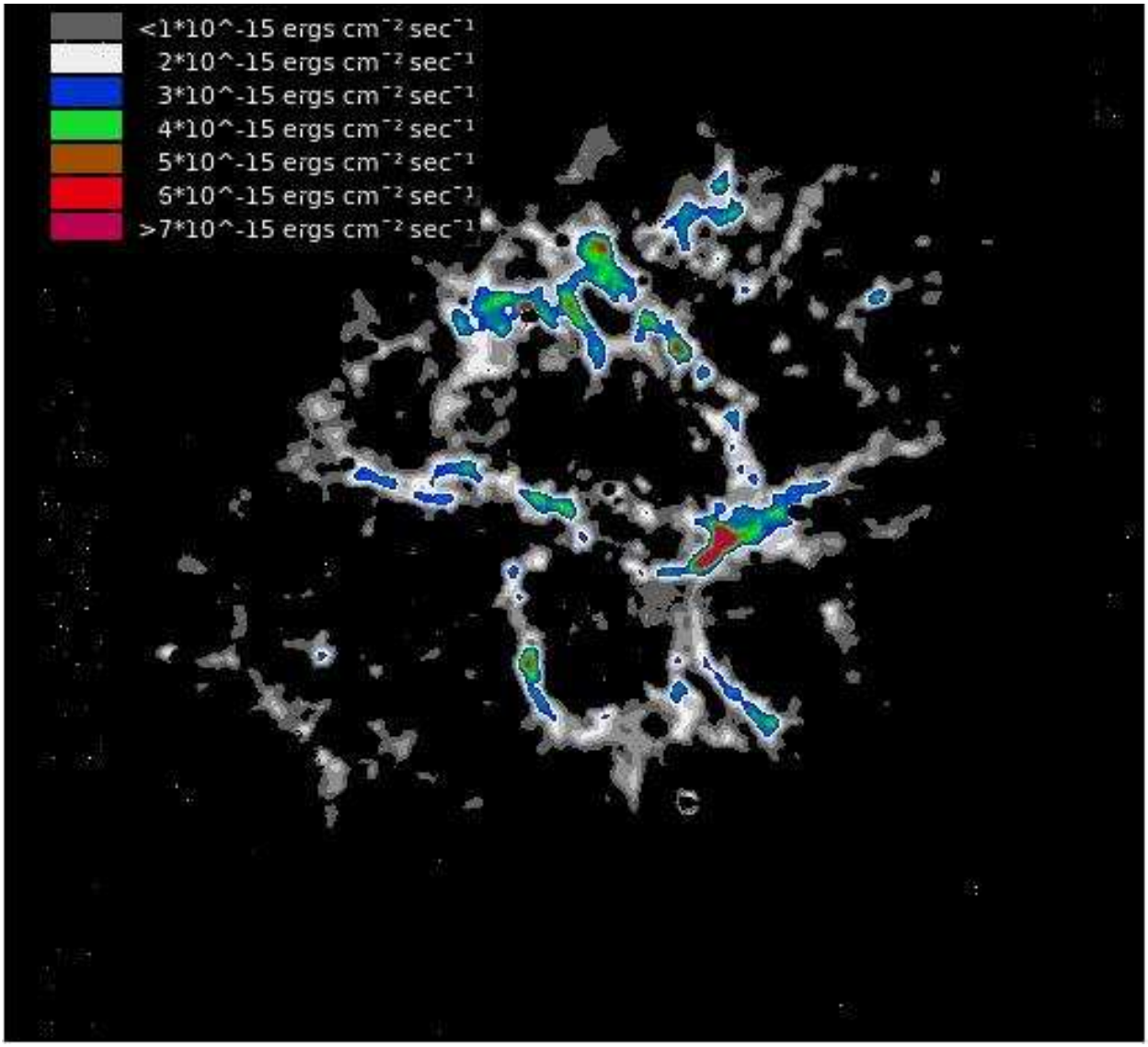

Fig. 12.— Flux Image of Hβ.

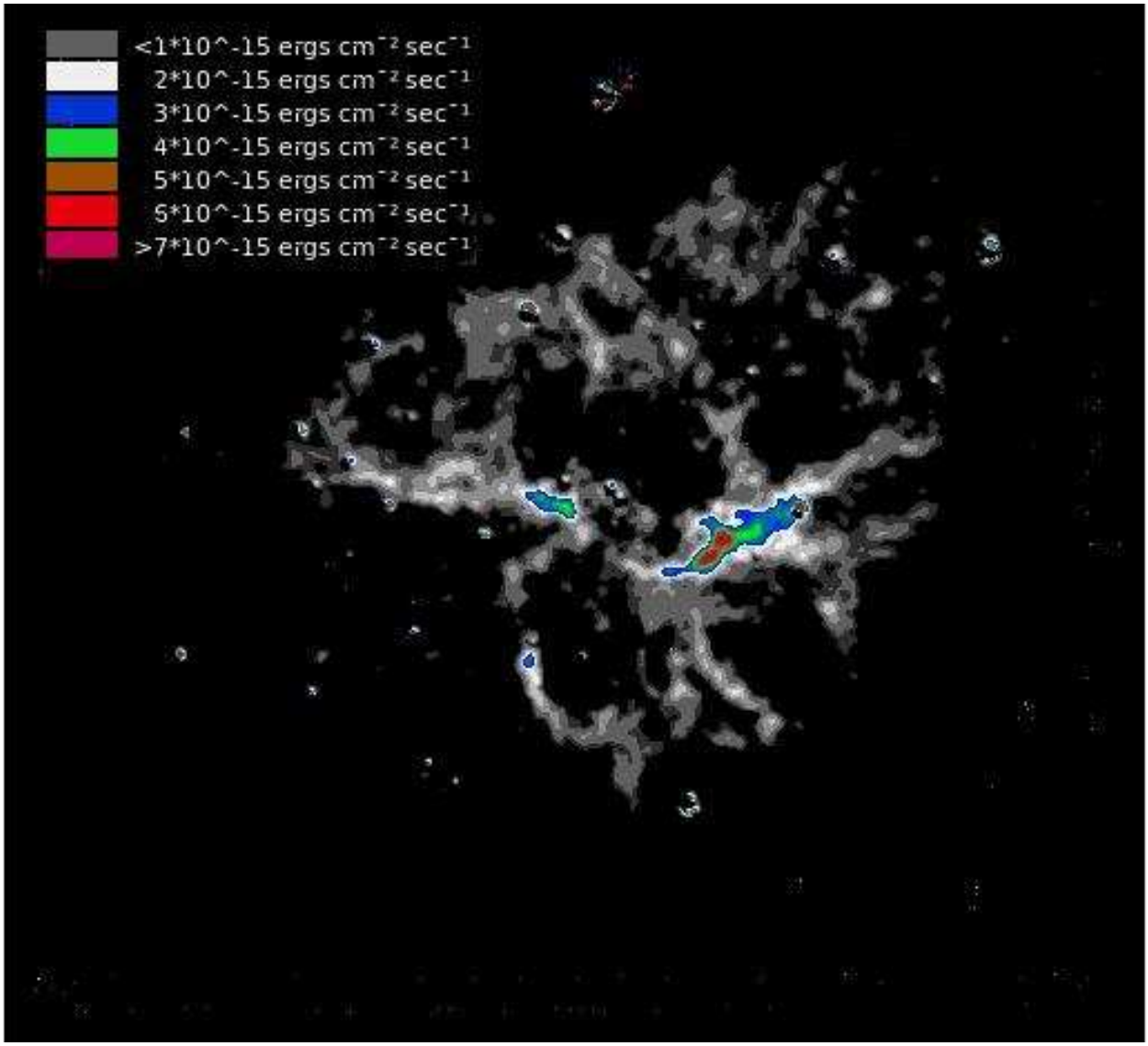

Fig. 13.— Flux Image of He I λ5876.

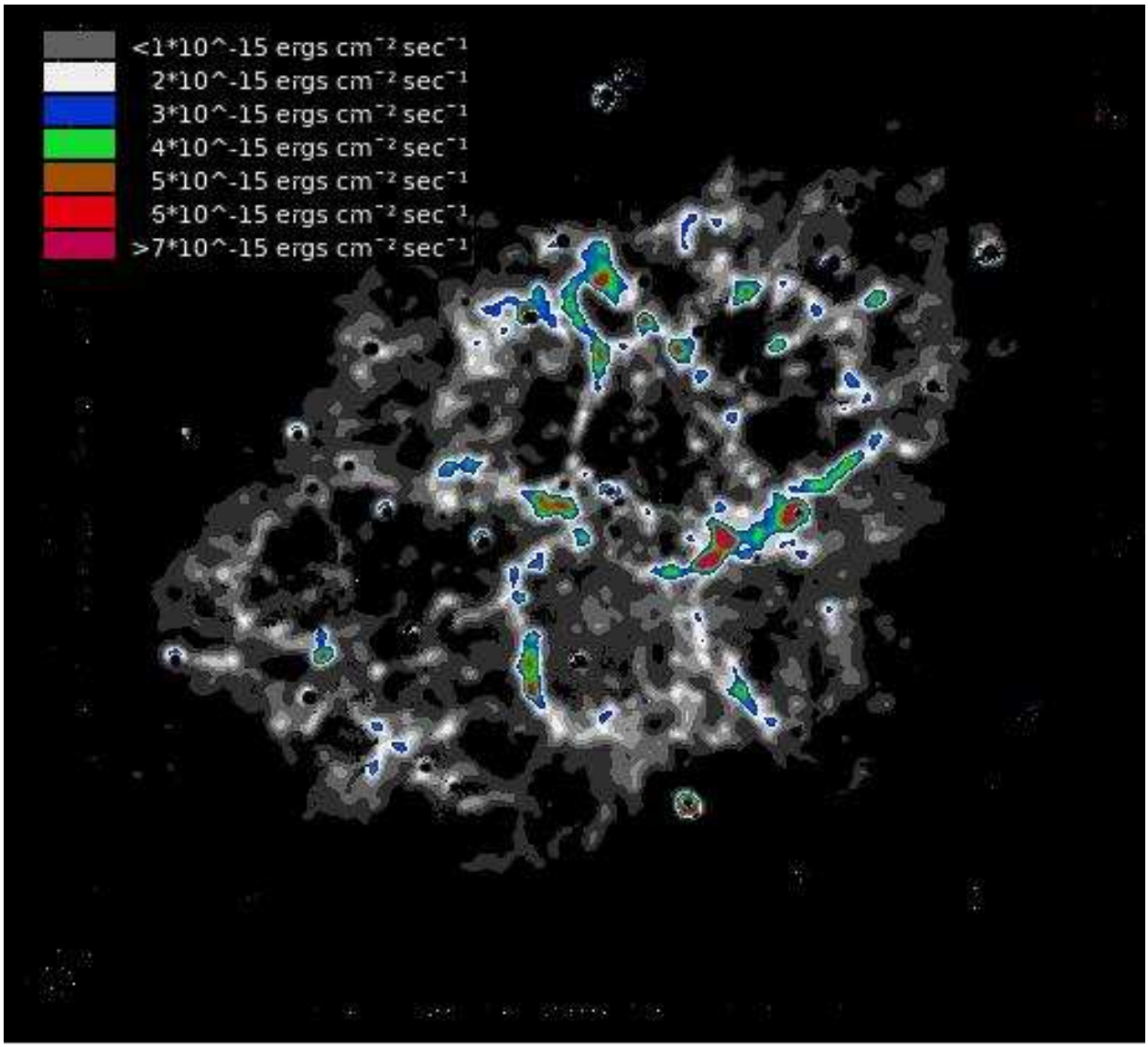

Fig. 14.— Flux Image of [O I] $\lambda\lambda$6300,6364.

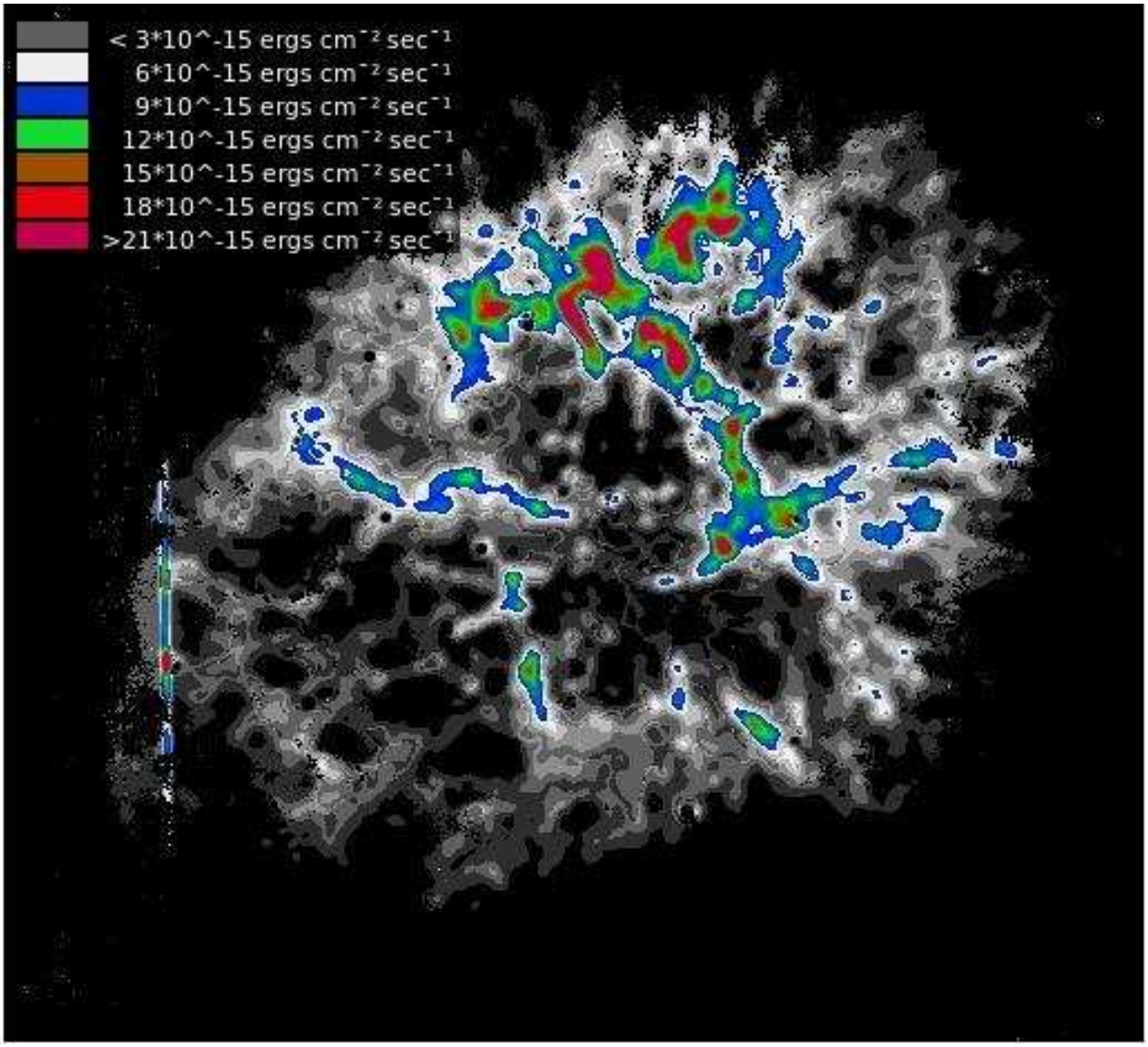

Fig. 15.— Flux Image of [N II] $\lambda\lambda$6548,6583.

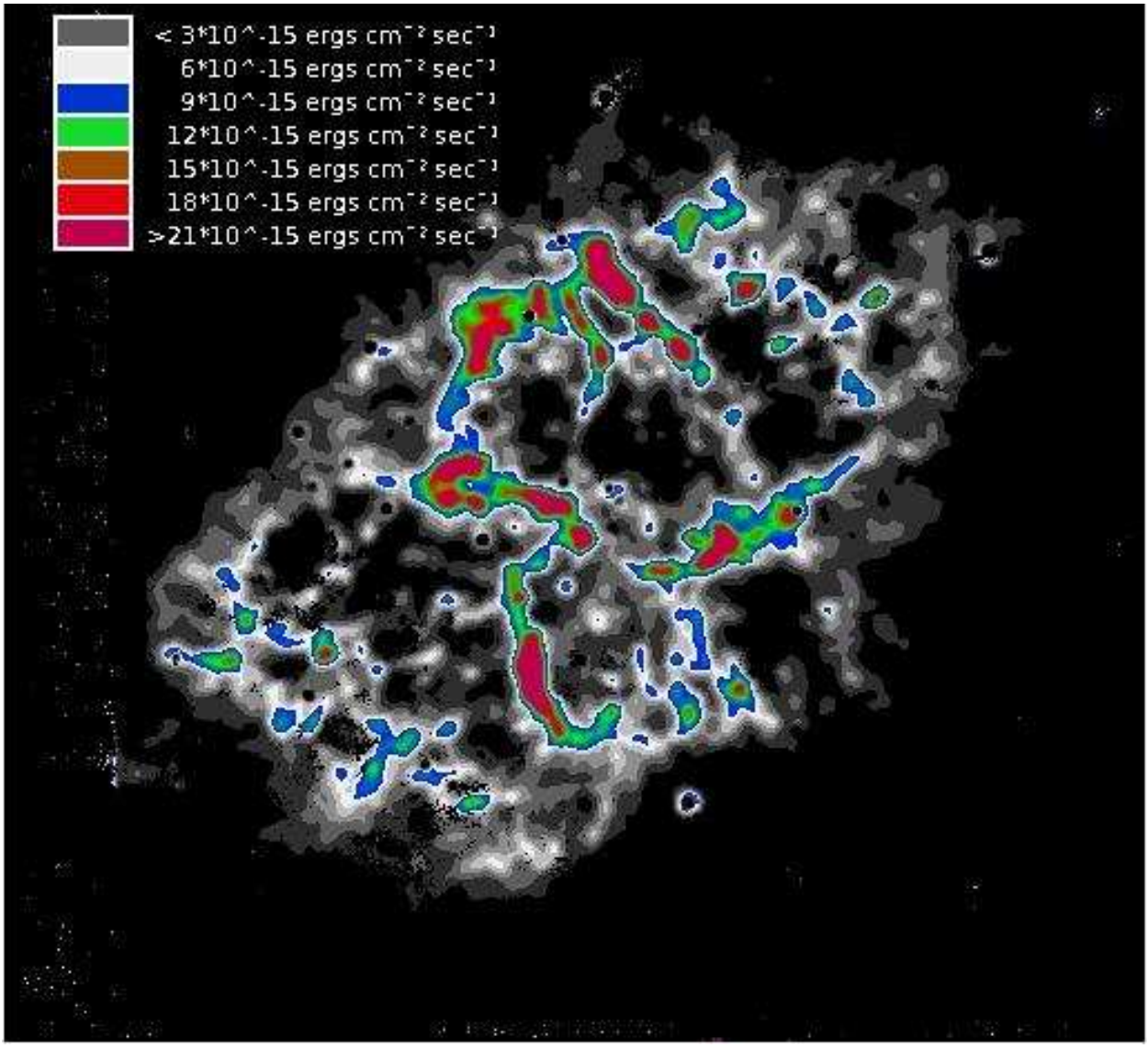

Fig. 16.— Flux Image of [S II] $\lambda\lambda$6716,6731.

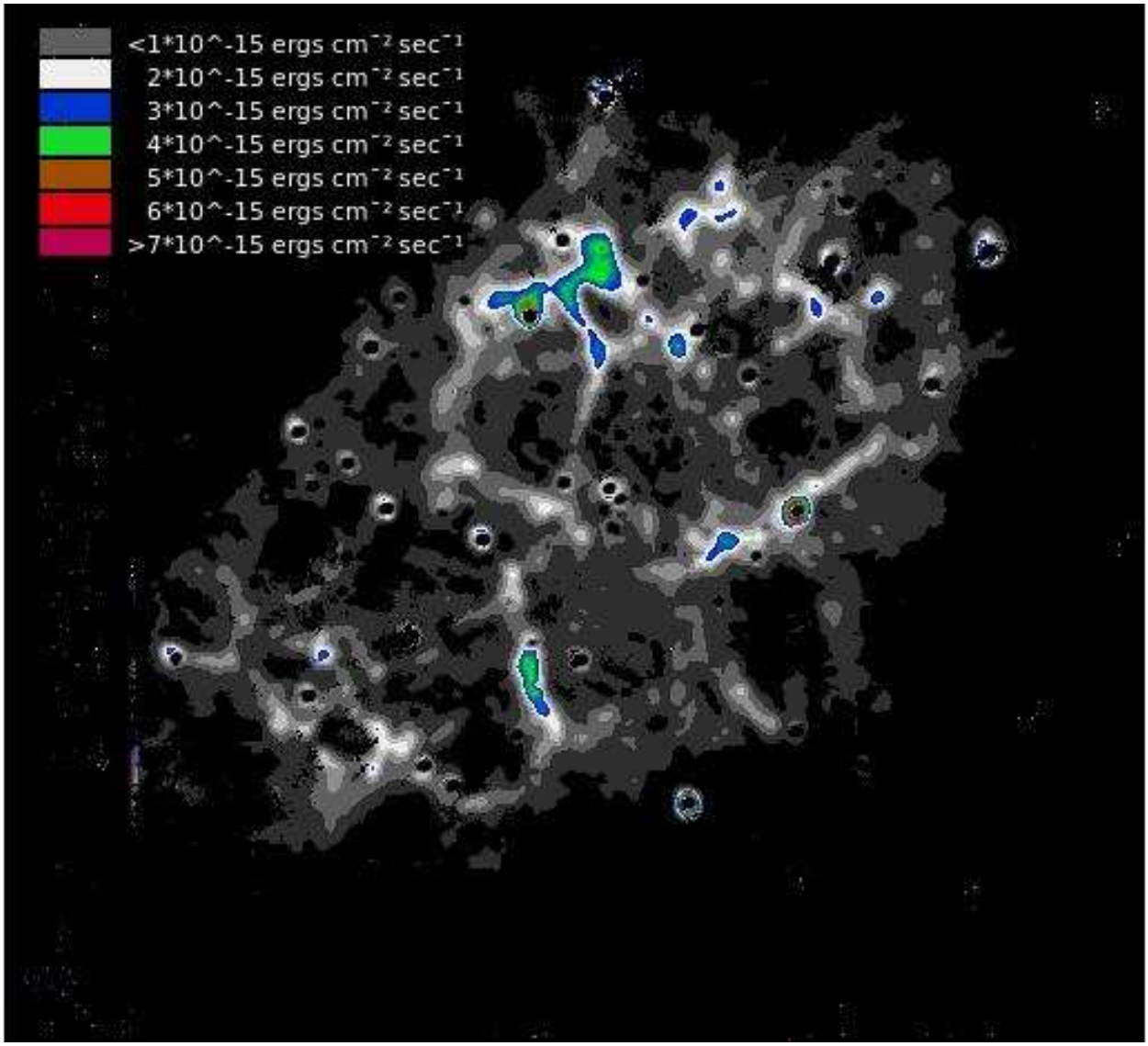

Fig. 17.— Flux Image of [Ni II] λ7378.

4. Mapping the Elemental Abundances

To map the spatial distributions of the elements in the Crab Nebula, we need both emission-line flux observations (which we obtained as described above) as well as simulated flux outputs from different model calculations. To compare our line fluxes with the photoionization code, we divided through all of our images with our Hβ map, which at first provided misleading values for pixels with a very low signal to noise ratio. Because of this, we set all pixels in our flux ratio images to zero that had a S/N ratio of less than 5 in our Hβ image. This eliminated the misleading pixel values. These relative line ratio images can be seen in Figures 18-23.

As noted before, we used the photoionization code Cloudy c08.00 (Ferland et al. 1998) to simulate different filament compositions as well as the physical properties of the Crab Nebula. By changing the elemental abundances in our models, we created different sets of emission lines with different intensities. These calculated emission line sets can be compared to our observations for each pixel, enabling us to find the model that comes closest to matching observations. We then assigned the abundances from that model to the corresponding pixel. We ran 6600 "nested" abundance models with differing helium, nitrogen, oxygen, and sulfur. Within each model of helium, which had discrete values for the helium mass fraction from 40% to 93%, we had abundance groups of nitrogen which varied the mass fraction from 0.25 times solar to 2.5 times solar in increments of 0.25. Oxygen mass fraction model groups were nested within each nitrogen abundance, and these were varied from one times solar to 19 times solar, in increments of 2. Finally, sulfur mass fraction model groups that simulated from 1 times solar to 6 times solar in increments of 0.5 were nested within each oxygen abundance. These values are meant to span the minimum and maximum values for the abundances of the models that matched the spectra in Sec. 2, and included higher abundances which will allow us to simulate emission ratios that

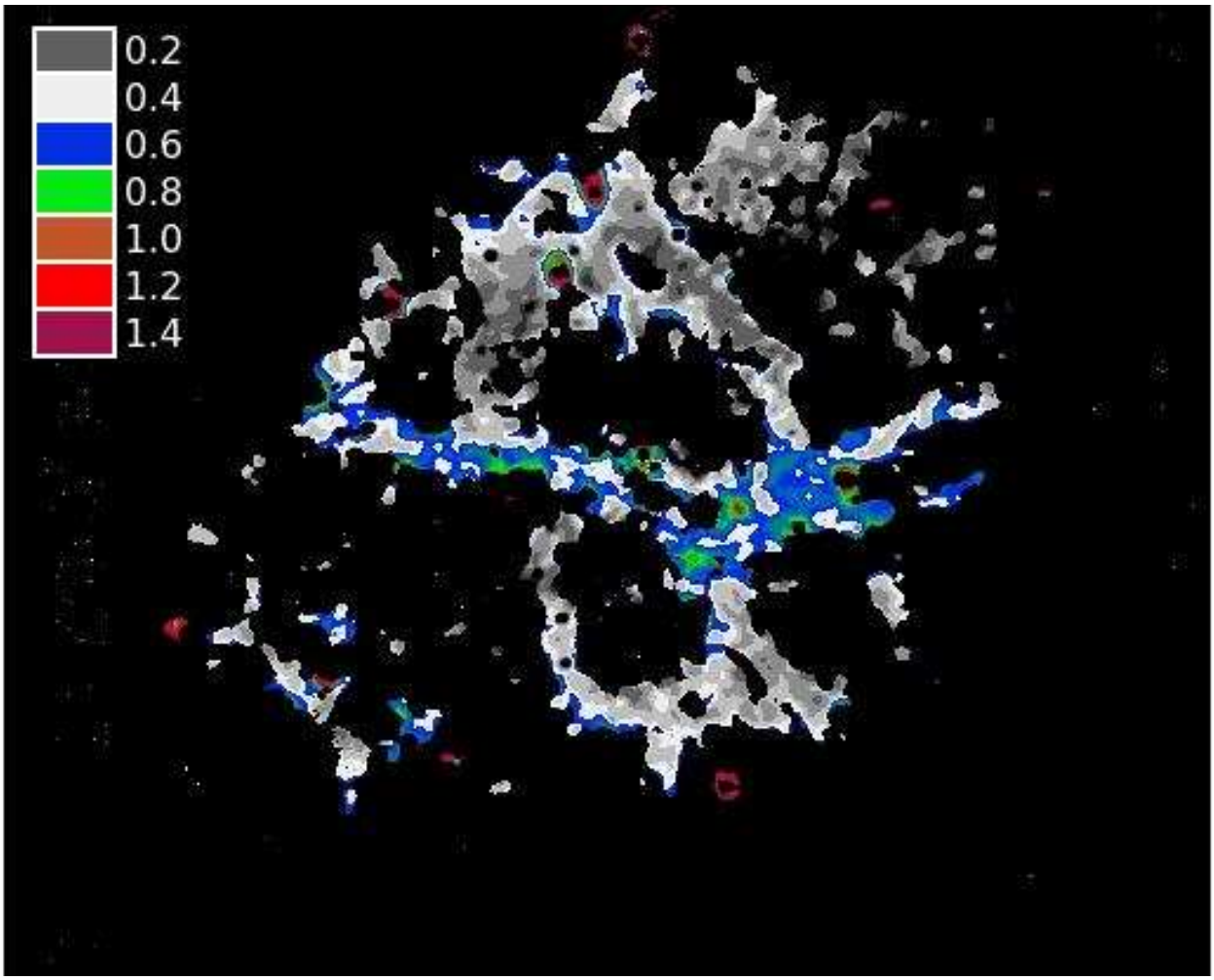

Fig. 18.— Flux Ratio Image of He II λ4686/Hβ.

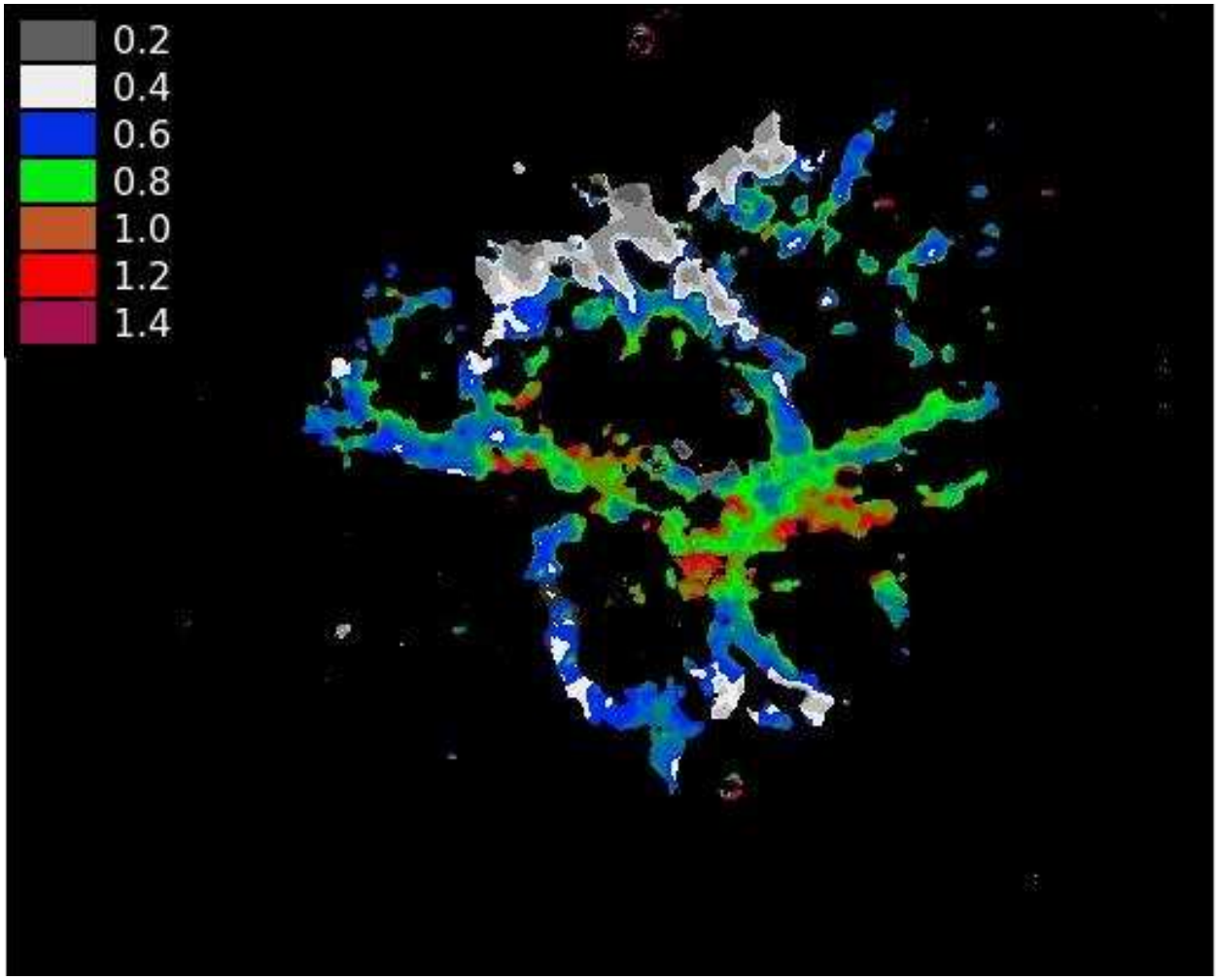

Fig. 19.— Flux Ratio Image of He I λ5876/Hβ.

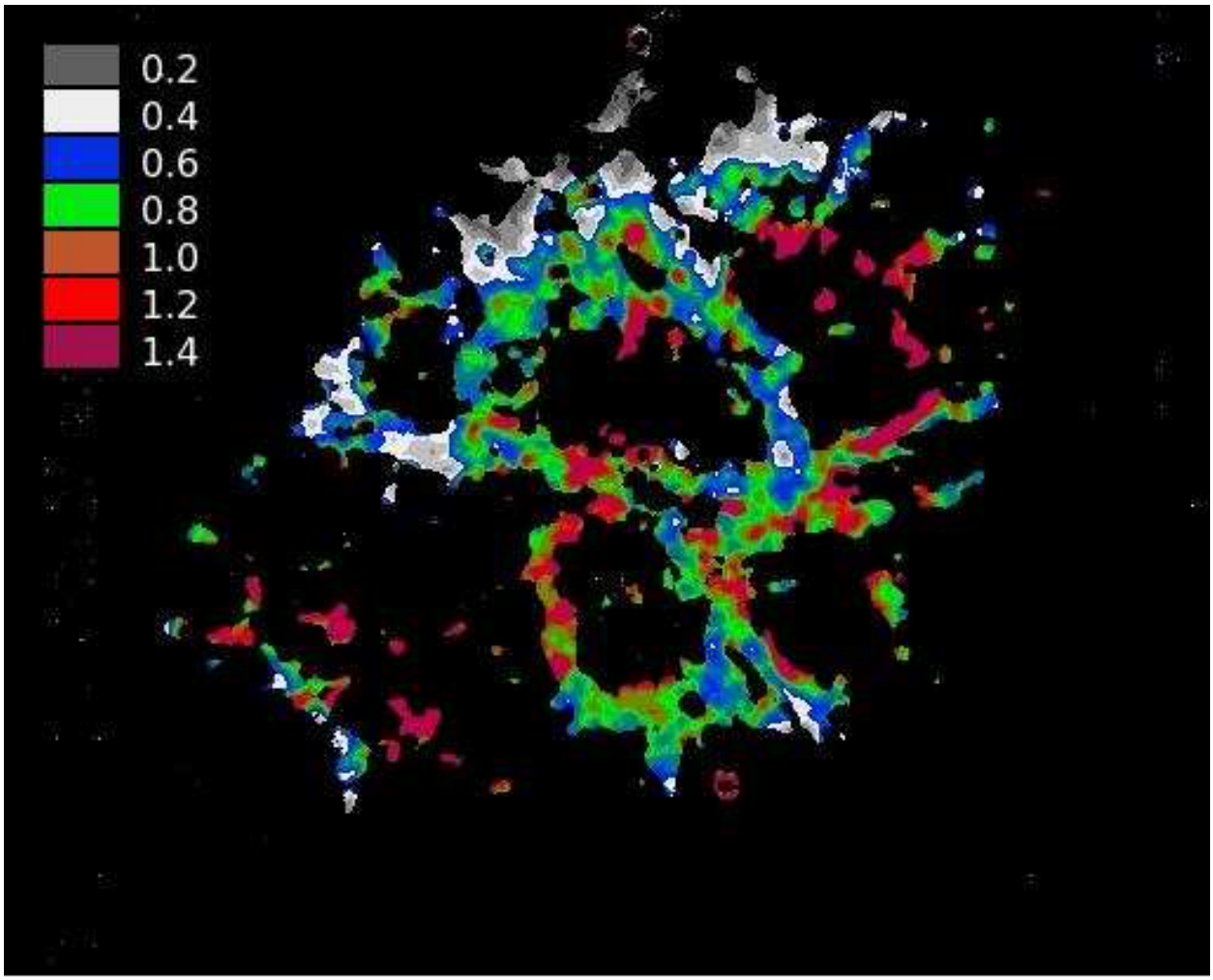

Fig. 20.— Flux Ratio Image of [O I] $\lambda\lambda$6300,6364/Hβ.

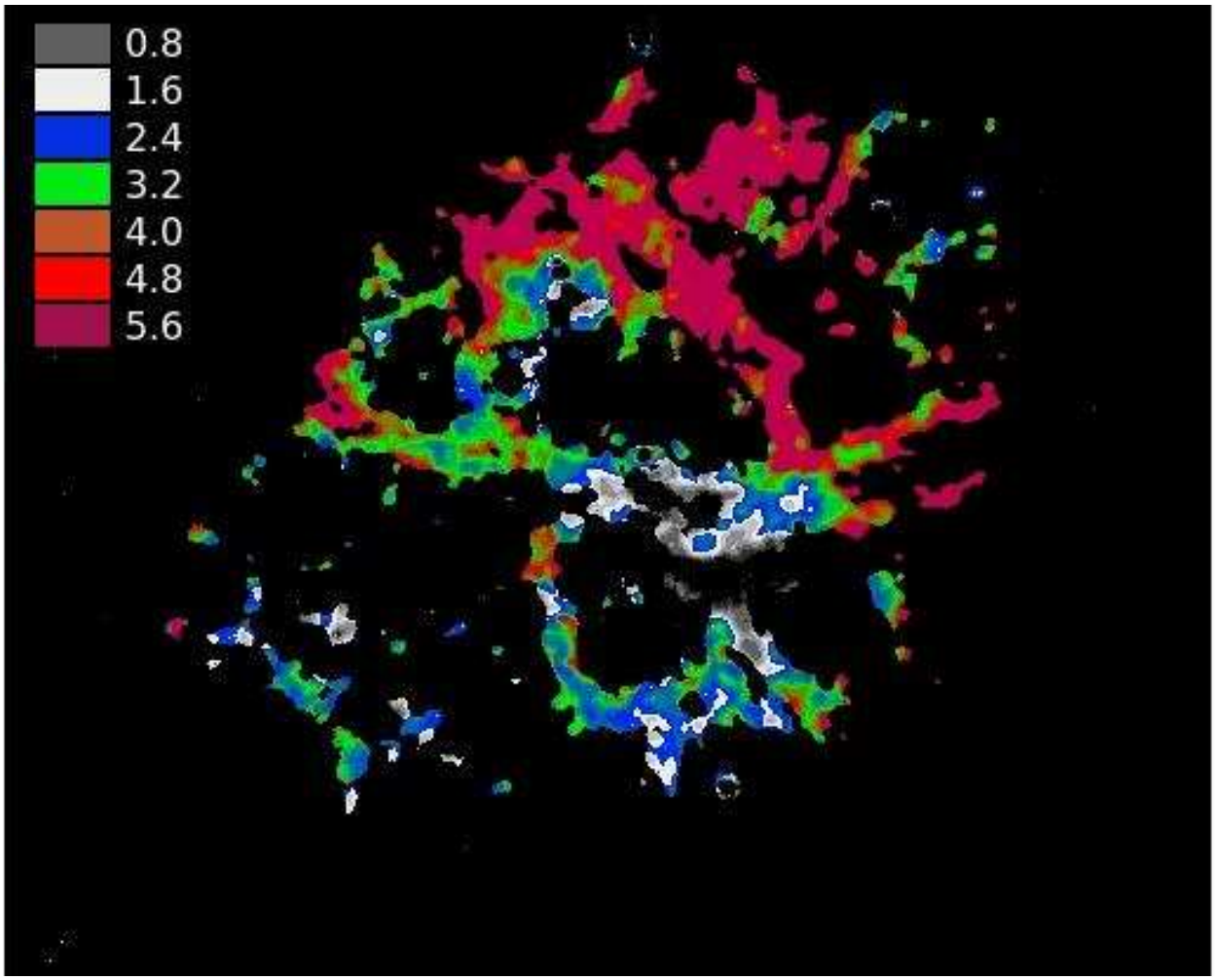

Fig. 21.— Flux Ratio Image of [N II] $\lambda\lambda$6548,6583/Hβ.

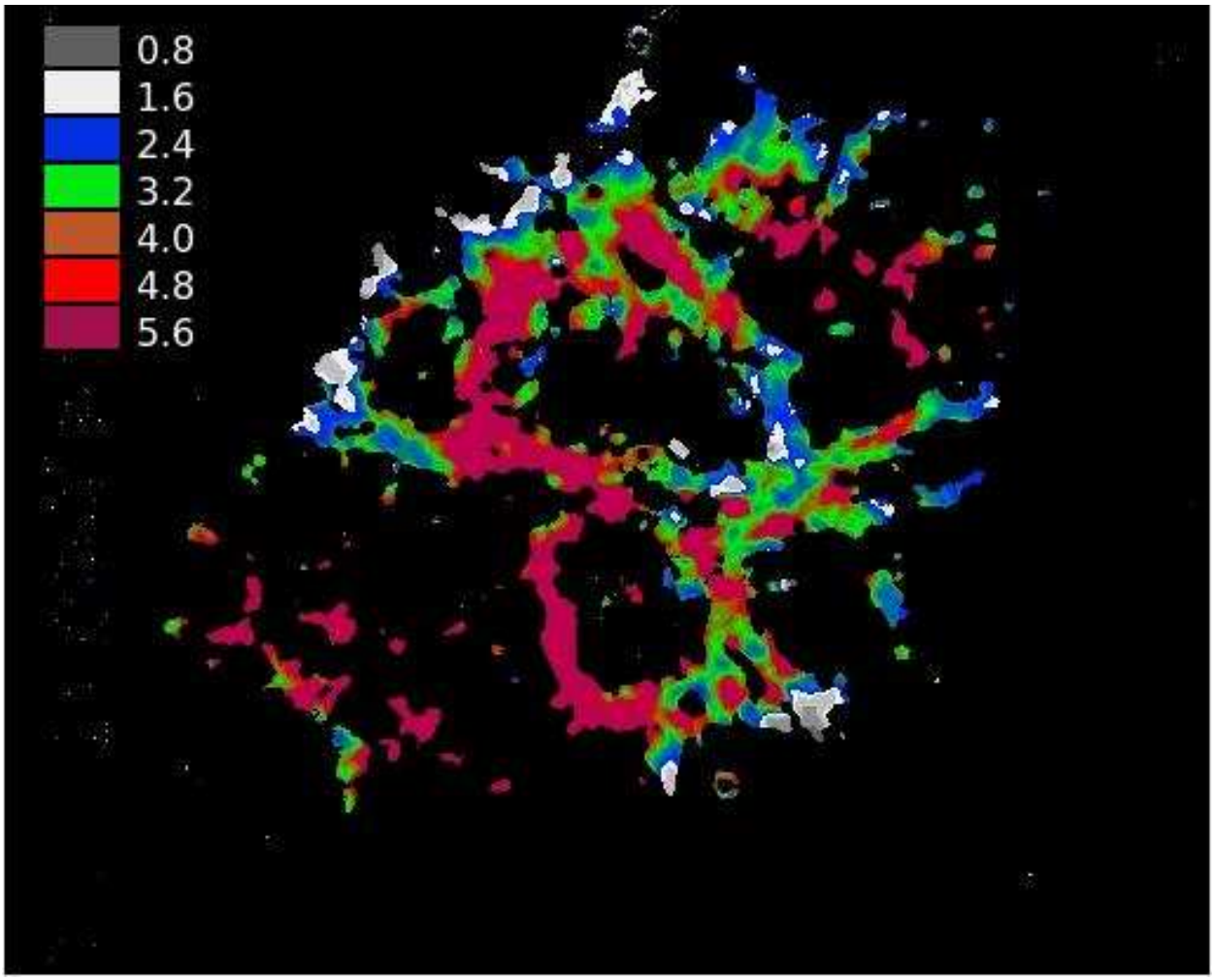

Fig. 22.— Flux Ratio Image of [S II] $\lambda\lambda$6716,6731/Hβ.

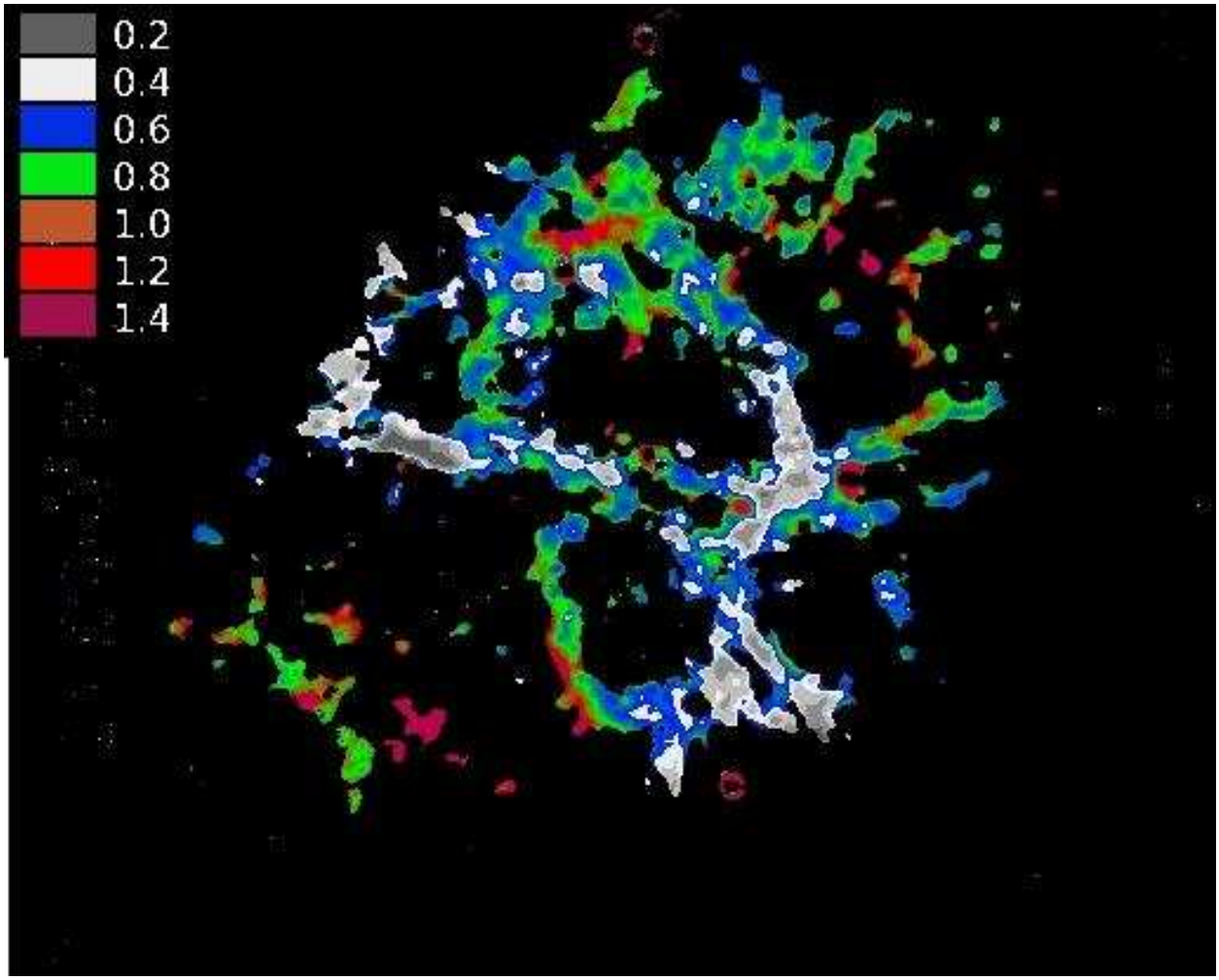

Fig. 23.— Flux Ratio Image of [Ni II] λ7378/Hβ.

are greater than the range we previously investigated using median measured spectra. We initially used a value of 3000 cm^{-3} for the hydrogen density, a log ionization parameter of -3.2, and an ionizing spectrum that is similar to the one provided by the Cloudy code for all of our models; these are the values that best matched emission line observations in Domains 1 and 2 in Sec. 2. We then obtained sets of theoretical line-emission ratios at three times the distance into the cloud where H and H^+ have equal ionization fractions. This distance was chosen because there is no more substantial emission of any line of interest beyond this distance into the cloud (see Figures 5-9).

After obtaining line ratios from these nested models, we developed a program to connect each pixel to a model that most closely matches the observations at that particular pixel. To develop an effective program for doing this, we first determined which elemental abundances have the most effect on the emission lines we calculated. We found that He I λ5876 line emission is mostly independent of all of the non-helium mass fractions. As discussed in Sec. 2, helium mass fraction substantially affects other line intensity ratios. Other elemental mass fractions (nitrogen, oxygen, sulfur) did not greatly impact the production of lines other than the ones generated by their own ions. Because of this property, our program first determined the model of He I λ5876 emissions that came closest to matching observations of the He I λ5876 line at each pixel. The pixel was assigned the helium mass fraction from the matched model. We then compared observations with calculated [N II] $\lambda\lambda$6548,6583 emissions from models that had the helium mass fraction assigned to the pixel. We assigned each pixel the nitrogen mass fraction from the model that came closest to matching [N II] observations. Using similar methods, we also compared simulated [O I] emission with observations to determine oxygen mass fraction and then compared [S II] observations with the smallest set of models (using the determined He, N, and O mass fractions to restrict the set). After these calculations, each pixel corresponded to a specific abundance set, and these abundances were read into an image for each element

of interest. We also wanted to create a nickel abundance map, but the Cloudy code did not produce calculations for the [Ni II] λ7378 line. However, Cloudy does generate enough information for us to determine the nickel emission ratio indirectly. Production of the nickel map is being planned as a future project.

Our first set of images contained some inconsistencies. After examining our sulfur abundance maps, we found that we simulated high sulfur in areas where we saw low sulfur emission, and we also modeled low sulfur where we observed high emission. After carefully examining and debugging our code, we realized that we had overlooked contributions from [N II] λ6548, [O I] λ6364, and [S II] λ6716 lines in our model calculations, all of which were transmitted through our interference filters. We also changed our log ionization parameter from -3.2 to -3.5 to compensate for low modeled [S II] and [O I] emission like we did for Domain 3 in Sec. 2. We then generated a new set of improved abundance maps with these changes, which can be seen in Figures 24, 25, 26 and 27.

4.1. Analysis of the Abundance Maps

As expected, the abundance distributions resemble the line ratio (to Hβ) maps in Figures 19-22, which were used for comparison with the photoionization models. The strong influence of the helium abundance distribution (discussed in Sec. 2) can also be seen in the map for nitrogen.

There is a high helium mass fraction throughout the Crab Nebula. However, there are significant variations in these mass fractions. For example, we model only 45% to 80% helium in most of the northern lobe and more than 94% helium in the western part of the central region, as seen in Fig. 24. This eliminates the efficiently emitting [N II] zone that was discussed in Sec. 2, and thus a higher nitrogen mass fraction is required to produce the

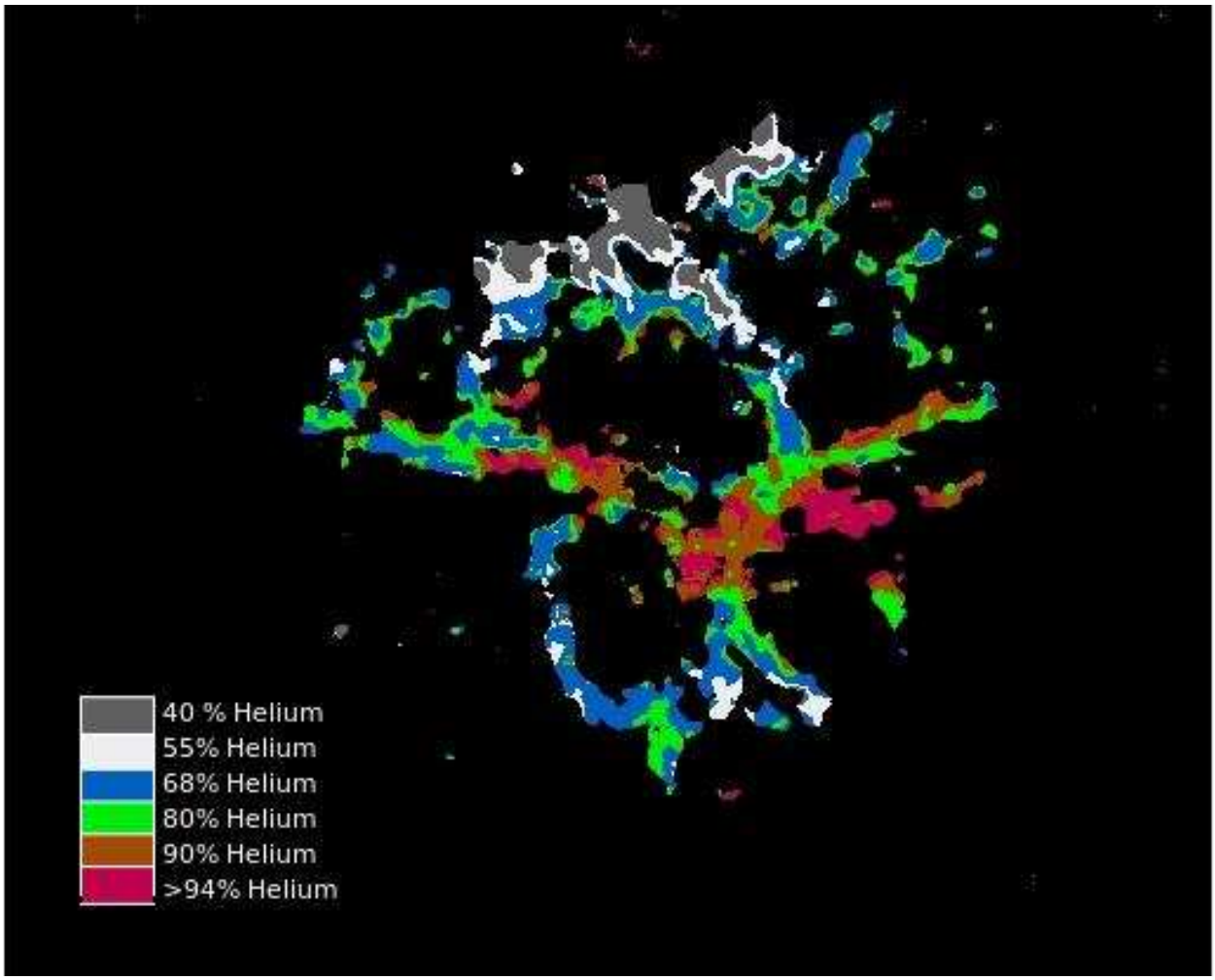

Fig. 24.— Map of Helium Abundance.

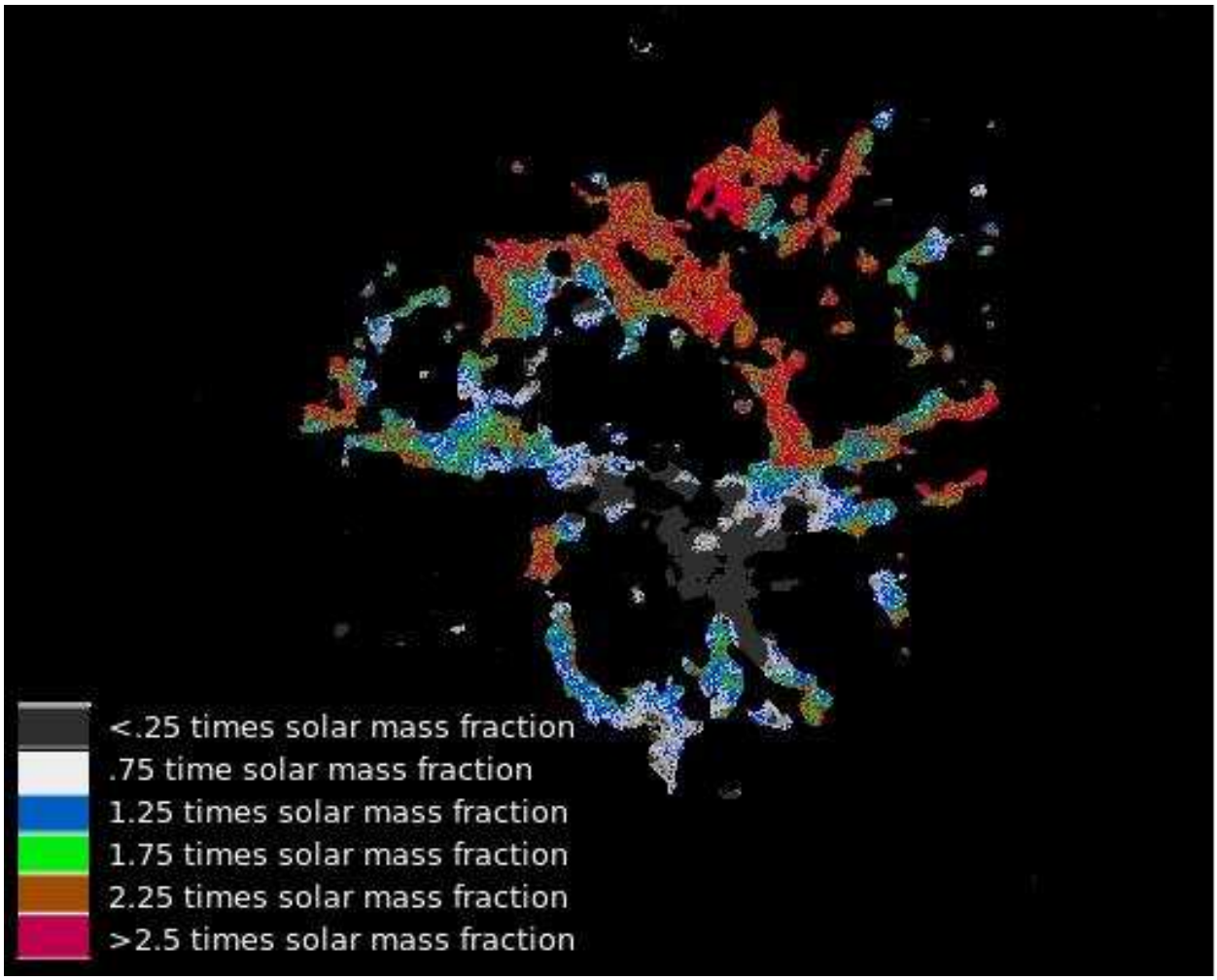

Fig. 25.— Map of Nitrogen Abundance.

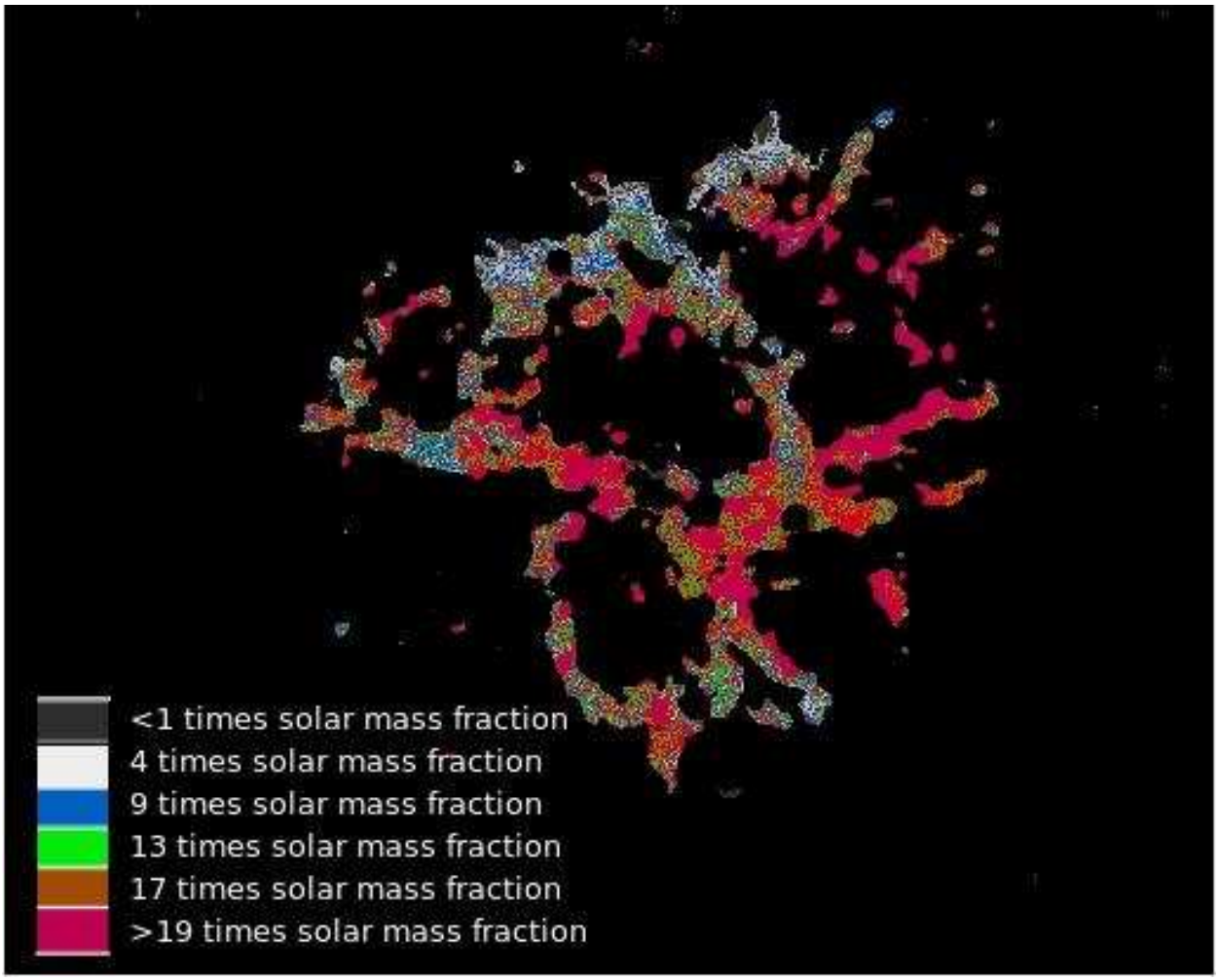

Fig. 26.— Map of Oxygen Abundance.

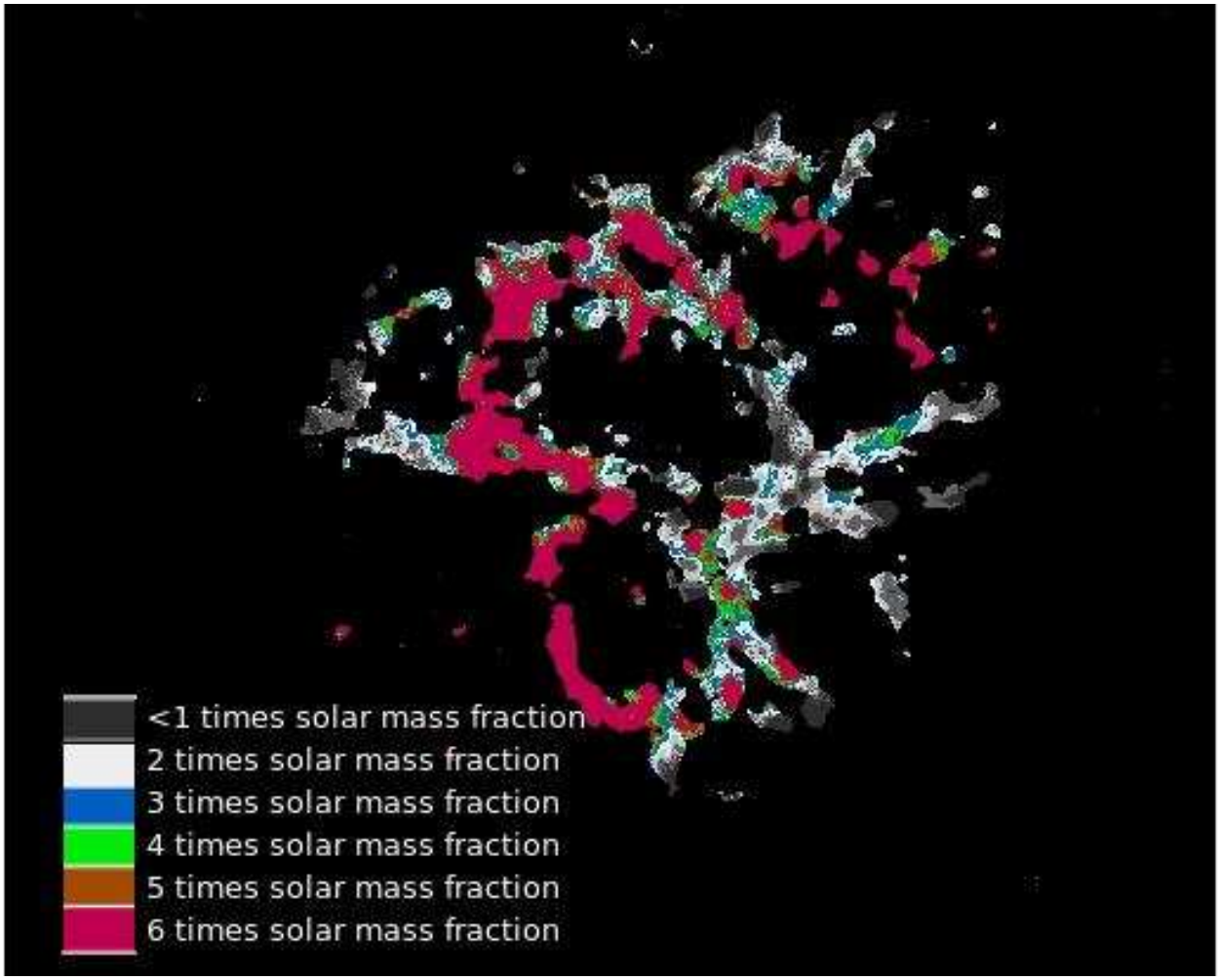

Fig. 27.— Map of Sulfur Abundance.

observed [N II] emission. While this range is lower than the helium mass fraction of Domain 1 in Sec. 2, the conclusions made in Sec. 2 used a median spectrum, which may not be exactly representative of the emission seen in the northern lobe. The helium in the northern lobe gives evidence for gas that had just finished CNO processing and was transitioning into the helium-burning process. We also observe strongly enhanced helium in the central east-west region and helium slightly less enhanced in the southern lobe. This suggests more advanced stages of processing have occurred in these areas.

High nitrogen in a region should be an indicator of CNO processed gas or gas that has just begun helium burning. We modeled high abundances of nitrogen in the northern lobe of the Crab Nebula, as seen in Fig. 25. When we combine that with our distribution for helium, it strongly argues for stellar processing that was finishing CNO processing and was just beginning helium burning. We also see roughly solar or depleted nitrogen in most of the central region and the southern lobe, which further supports the idea that more advanced stages of processing have occurred.

Oxygen should give us information on where processing reached an advanced stage of helium burning. When we examine the oxygen abundance map, we see high oxygen represented throughout the Crab Nebula, shown in Fig. 26. Strong abundance enhancements of oxygen in the central region and southern lobe indicate that the nebular gas had at least been processed through helium burning. The northern lobe has less oxygen than in the central lobe, which again suggests that helium burning was just beginning in this zone, as large oxygen abundances are not expected until later helium burning stages (see Figure 2).

The sulfur distribution in Fig. 27 is very asymmetric. We see very little sulfur enhancement in the southwestern part of the Crab Nebula, and sulfur abundances are high in the northeastern and southeastern part. Note that we model high sulfur in a zone where

we found relatively low helium and high nitrogen, which does not agree with standard elemental processing theory. The most likely explanation for this distribution of sulfur is that it was generated by an off-center oxygen flash (the products were probably originally deposited in the eastern part of the central region). Some of the sulfur was then driven out into other filaments (i.e. the northern and the southern lobe) by a N-S relativistic wind coming from the pulsar (see Fig. 4 of Michel et al. 1991). This sulfur abundance distribution indicates that oxygen burning occurred in the precursor, which argues for a precursor star with a mass of at least 10 $M_{\odot}$.

5. Results and Discussion

The photoionization calculations presented in Section 2, when matched with spectra from (MacAlpine et al. 2007), were used to analyze three regions expected to represent theoretical stellar elemental processing stages in the Crab Nebula.

Domain 1: Simulations from the domain with the highest nitrogen emission lines have a helium mass fraction of 89%, solar nitrogen and carbon and oxygen, with depleted sulfur. While this was previously thought to be gas processed only through the CNO cycle, solar nitrogen in this domain suggests either substantial gas mixing or that helium burning had begun to occur, depleting nitrogen.

Domain 2: A large amount of the emitting nebular gas, with a [N II] λ6583 to Hα ratios of 1–2.5, is determined to have 89% helium mass fraction. Nitrogen is about a third of its solar value, and carbon is six times solar. Sulfur and argon have about a fourth to half of their solar values. This nitrogen depletion, in addition to high carbon, indicates that this gas has undergone helium burning.

Domain 3: Simulations representing the domains that have high sulfur emission and

low nitrogen emission also have a measured helium mass fraction of about 89%. Nitrogen is further depleted; its mass fraction is about a fourth of solar. Carbon and oxygen mass fractions are ten times solar, while argon and sulfur mass fractions are enhanced by six times and four times solar, respectively. This represents what we expect to be the results of oxygen burning, but high oxygen and carbon also suggest that some mixing has occurred in this region as well.

Gas resulting from the CNO cycle and gas processed through oxygen burning had been previously considered by MacAlpine et al. (1996). Our calculations show that strong [N II] does not necessarily imply high nitrogen abundance, due to the warm nitrogen emitting zone caused by high helium abundance. However, because [C I] λ9850 is produced by $C^+ \rightarrow C^0$ recombination and subsequent collisional excitation, high emission of this line does suggest high carbon abundance. The implication of solar or lower nitrogen and enhanced carbon throughout the nebular gas suggests a precursor star with a mass that exceeds 9.5 $M_\odot$.

We obtained new observations with custom emission-line filters to find the spatial distributions of elements in the Crab Nebula. Our methods for reducing images and eliminating continuum were also discussed. Modifying the equations in Jacoby et al. (1987), we were able to subtract accurately the continuum images for each wavelength of interest, and we also were able to deal with line contamination of Hα and the fact we had doublet lines that passed through the filters. Using Fabry-Perot images, we assigned an accurate velocity distribution to each pixel, and then used the resulting redshifts and blueshifts of lines to deal correctly with the expanding nebula. This eliminated up to a ten percent error in the flux images.

Our code allows us to match line intensity ratio observations with abundance models, and we created abundance maps of four different elements. Inspection of our maps indicates

that the northern lobe consists of gas that had probably just entered helium burning. We also found that most of the Crab Nebula does contain high helium abundance, as well as other products from various stages of helium burning. Further, the presence of high sulfur distributed asymmetrically suggests that an off-center oxygen flash took place before the supernova event (see Woosley & Weaver 1995). In addition, the fact that there is high sulfur directly northeast and southeast of the pulsar suggests that sulfur was repositioned in the filaments by a relativistic wind. Since we see evidence for oxygen burning in the Crab Nebula, we can put a new lower mass limit of 10 $M_{\odot}$ on the precursor star. Work done by Nomoto (1985) states that a Mg-Ne-O core collapse can only come from a star with a mass less than 10 $M_{\odot}$. When we combine this information with the work done by Wanajo et al. (2009) which further suggests that the Crab Nebula came from a Mg-Ne-O core collapse, we can argue consistently for a precursor star of 10 $M_{\odot}$ that underwent a Mg-Ne-O core collapse.

A. Appendix

This is an appendix describing work done for support of our primary analyses. These results can also be used for future studies of the Crab Nebula by others.

A.1. Photometry of Stars in the Field of the Crab Nebula

To perform the necessary data reductions mentioned in Sec. 3, we needed photometric nights. If clouds were present on the nights we obtained our observations, we would not be able to obtain accurate sensitivity values for our images due to absorption by a non-uniform cloudy layer. To enable calibration of our images in the case of a variable, nonphotometric night, we performed photometry on the stars in the field of the Crab Nebula that could serve as standard stars. To do this, we used images taken by Gordon MacAlpine in 1998 November with the Hiltner 2.4 m telescope and the Echelle CCD camera at MDM observatory. To photometrically calibrate an object, the summed count rates from that object (in this case the stars in the field of the Crab Nebula) were converted to a magnitude (a measure of star brightness) on the standard UVBRI photometric system. After performing data reduction using methods similar to those described in Section 3.1 and median filtering the images for each set of filters, one aperture was placed around a star with an aperture radius that was approximately three times the full width half maximum of the star's stellar profile. This provided us with the number of counts in an area that contained emission from both the star and the night sky. Another aperture with an inner radius five times larger than the radius of the star being measured was placed around the object to measure the average number of background counts in the sky per pixel. Using both of these measurements, we were able to determine the number of counts the star contributed to the image. The counts were then converted to instrumental magnitudes. This was done for each of the filters to determine BVRI magnitudes. All of the aperture

photometry was performed by the IRAF package *daophot*.

After finding the instrumental magnitudes for both the photometric standard stars and our object stars (the stars in the field of the Crab Nebula), we had to account for both the airmass extinction factor (which varies for each filter), as well as the fact that the CCD camera does not exactly match the camera used for measuring the official UVBRI standards. Because the standard stars have their UVBRI data published by Landolt (1983), we could determine the coefficients of the equations (where mB, mV, mR, mI, are all instrumental magnitudes):

$$mB = (BV + V) + b1 + b2 * Airmass + b3 * BV \tag{A1}$$

$$mV = V + v1 + v2 * Airmass + v3 * BV \tag{A2}$$

$$mR = (V - VR) + r1 + r2 * Airmass + r3 * VR \tag{A3}$$

$$mI = (V - VI) + i1 + i2 * Airmass + i3 * VI \tag{A4}$$

These equations are given in IRAF (Tody 1986). After solving these equations using the IRAF task *fitparams*, we inserted our instrumental magnitudes of our object stars and determined the actual magnitudes of the stars for each filter color used in the observations. The maximum magnitude of our errors was three hundredths of a magnitude, but most stars are good to within a hundredth of a magnitude. The magnitudes of the measured stars are in Table 5. We numbered the stars in the field using the numbering system of Wyckoff & Murray (1977).

Table 5. Photometry of Stars in the Field of the Crab Nebula

Star	V Magnitude	B-V	B-R	V-I
WM-2	15.560	1.240	0.714	1.521
WM-4	17.209	0.880	0.660	1.041
WM-5	16.178	0.872	0.547	1.224
WM-6	16.378	0.983	0.623	1.251
WM-7	14.980	0.656	0.372	0.930
WM-8	16.665	0.677	0.440	0.967
WM-9	14.393	1.217	0.743	1.459
WM-10	16.645	0.849	0.588	1.179
WM-11	16.929	1.065	0.791	0.805
WM-12	16.412	1.262	0.758	1.467
WM-13	16.297	0.838	0.629	1.200
WM-14	16.874	0.805	0.993	1.044
WM-15	17.753	0.809	0.682	1.101
WM-16	15.797	0.851	0.556	1.023
WM-18	16.858	0.811	0.595	1.447
WM-19	14.289	0.770	0.464	1.004
WM-21	15.458	0.872	0.566	1.174
WM-22	16.198	0.969	0.597	1.239
WM-23	15.801	0.690	0.511	0.982
WM-24	15.800	0.818	0.508	1.156

Table 5—Continued

Star	V Magnitude	B-V	B-R	V-I
WM-25	15.816	1.476	0.799	1.668
WM-26	15.364	0.417	0.229	0.596
WM-27	16.607	1.395	0.908	1.584
WM-28	17.129	0.797	0.568	1.151
WM-29	15.524	0.581	0.376	0.851
WM-30	15.575	0.719	0.543	1.004
WM-31	15.856	1.108	0.674	1.419
Crab Pulsar	16.566	0.597	0.474	1.051

Note. — Photometry measurements for stars in the field in the Crab Nebula.

A.2. Synchrotron Radiation vs. Shock Heating

If the Crab Nebula is collisionally ionized by shock heating rather than photoionized by synchrotron radiation, our models would not produce accurate ionization structure and line emission calculations, and all of the scientific analysis we have done in the previous sections would become invalid. One way to determine which process is taking place is to measure the temperature via emissions of different emission lines coming from the same ion. For shock heated gas, the electron temperature derived from [O III] lines would be $>3.0*10^4$ K, while we should measure a temperature of roughly 1.0-1.5*10^4 K for synchrotron heating (Osterbrock 1989). We can get the necessary emission-line information from spectra at different positions in the Crab Nebula.

For this analysis, we used long-slit spectra taken by Gordon MacAlpine on October 27-28, 1997 on the 2.4 m Hiltner telescope at MDM Observatory with the Templeton CCD. After the instrumental signature is removed from a long-slit spectroscopic image, a spectrum must be extracted before analysis can be performed. This involves selecting a region of coadded images for extraction as well as a background region for continuum subtraction. Geometrical distortions were present along the spatial axis, and these distortions were fixed with the IRAF task *fitcoords*. The spectrum is not a straight line along one column or line, but shifts slightly from pixel to pixel due to optical distortion. Because the Crab Nebula is an emission line object, we used comparison stellar spectra to find the effects this distortion had on the spectrum. Using the IRAF task *apall*, we performed all of these steps and extracted spectra for different positions in the Crab.

After the initial extraction, we calibrated for wavelength using a comparison exposure with known emission lines from an argon lamp, and used the IRAF task *identify* to mark specific positions on the comparison spectrum that corresponded to the lamp emission wavelengths. Using this information, wavelengths were assigned to different lines based on

their pixel position.

After wavelengths were calibrated, we then looked at the intensity ratios of [O III] $\lambda\lambda$4959+5007/[O III] λ4363. Because these two sets of emission lines come from different excitation levels (which depend heavily on temperature), we can use these ratios to measure the temperature in the Crab Nebula. Using the equation

$$\frac{j_{\lambda 4959} + j_{\lambda 5007}}{j_{\lambda 4363}} = \frac{7.73 e^{\frac{3.29 \times 10^4}{T}}}{1 + 4.5 \times 10^{-4} \frac{N_e}{T \cdot 5}} \tag{A5}$$

where j_λ is the amount of emission of a given line at wavelength λ, and T is the temperature of the filament, and N_e is the electron density (in $e\ cm^{-3}$), we could solve for the temperature in the Crab Nebula. We used values of N_e that corresponded to models run in Section 2, and the calculated temperatures are given in Table 6. The hottest temperature we measured in the Crab Nebula is in the range of (1.1-1.2)*10^4 K. This temperature is not hot enough to be consistent with ionization by shock heating. Thus, this spectroscopy confirms the idea that synchrotron radiation is ionizing the Crab Nebula and our models' ionization properties are valid.

Table 6. Measured Temperatures in the Crab by Spectroscopy

Position	$\frac{j_{\lambda 4959}+j_{\lambda 5007}}{j_{\lambda 4363}}$	Temperature, N_e=8000	Temperature, N_e=3000	Temperature, N_e=800
Crab-2	505.732	7795	7850	7860
Crab-8	564.268	7595	7640	7665
Crab-9	1036.98	6660	6695	6710
Crab-10	279.644	9075	9135	9160
CrabSkin-1	121.887	11800	11900	11925
CrabSkin-3	126.039	11650	11725	11760

Note. — Calculated temperatures (in Kelvin) for various nebular positions.

REFERENCES

Blair, W.P., Long, K.S., Vancura, O., Bowers, C.W., Conger, S., Davidsen, A.F., Kriss, G.A., & Henry, R.B.C. 1992, ApJ, 399, 611

Davidson, K., & Fesen, R. 1985, ARA&A, 23, 119

Ferland, G.J., Korista, K.T., Verner, D.A., Ferguson, J.W., Kingdon, J.B., & Verner, E.M. 1998, PASP, 110, 761

Fesen, R.A., & Kirshner, R.P. 1982, ApJ, 258, 1

Henry, R.B.C. 1986, PASP, 98, 1044

Henry, R.B.C., MacAlpine, G.M., & Kirshner, R.P. 1984, ApJ, 278, 619

Jacoby, G.H., Quigley, R.J., & Africano, J.L. 1987, PASP, 99, 672

Landolt, A.U. 1983, AJ, 88, 439

Lawrence, S.S., MacAlpine, G.M., Uomoto, A., Woodgate, B.E., Brown, L.W., Oliversen, R.J., Lowenthal, J.D., & Liu, C. 1995, AJ, 109, 2635

MacAlpine, G.M., McGaugh, S.S., Mazzarella, J.M., & Uomoto, A. 1989, ApJ, 342, 364

MacAlpine, G.M., & Uomoto, A. 1991, AJ, 102, 218

MacAlpine, G.M., Lawrence, S.L., Sears, R.L., Sosin, M.S. & Henry, R.B.C. 1996, ApJ, 463, 650

MacAlpine, G.M., Ecklund, T.C., Lester, W.R., Vanderveer, S.J., & Strolger, L.G. 2007, AJ, 133, 81

MacAlpine, G.M., & Satterfield, T.J. 2008, AJ, 136, 2152

Massey, P. & Foltz, C.B. 2000, PASP, 112, 566

Michel, F.C., Scowen, P.A., Dufour, R.J., & Hester, J.J. 1991, ApJ, 368, 463

Nomoto, K., 1985, in The Crab Nebula and Related Supernova Remnants, ed. M. Kafatos & R.B.C. Henry (Cambridge: Cambridge Univ. Press), 97

Oke, J.B. 1990, AJ, 99, 1621

Osterbrock, D.E. 1989, Astrophysics of Gaseous Nebulae and Active Galactic Nuclei (Mill Valley: University Science Books)

Tody, D. 1986,"The IRAF Data Reduction and Analysis System" in Proc. SPIE Instrumentation in Astronomy VI, ed. D.L. Crawford, 627, 733

Wanajo, S., Nomoto, K., Janka, H.-T., Kitaura, F.S. & Muller, B. 2009, AJ, 695, 208

Woosley, S.E., & Weaver, T.A. 1995, ApJS, 101, 181

Wyckoff, S., & Murray, C.A. 1977, MNRAS, 180, 717